IEEE Access
Multidisciplinary | Rapid Review | Open Access Journal

Received August 1, 2019, accepted August 2, 2019, date of publication August 6, 2019, date of current version August 21, 2019.

Digital Object Identifier 10.1109/ACCESS.2019.2933407

Sensorless Fault-Tolerant Control Strategy of Six-Phase Induction Machine Based on Harmonic Suppression and Sliding Mode Observer

YIWEN GENG[1], ZOU LAI[1], YONGGANG LI[1], DING WANG[1], RUICHENG CHEN[2], AND PENGFEI ZHENG[1]

[1]School of Electrical and Power Engineering, China University of Mining and Technology, Xuzhou 221116, China
[2]China University of Mining and Technology Xuhai College, Xuzhou 221116, China

Corresponding author: Zou Lai (laizou1002@163.com)

ABSTRACT This paper deduces a unified mathematical model of open-circuit fault of six-phase induction machine, and purposes a fault-tolerence sensorless strategy based on the sliding mode observer(SMO) to estimate the rotor flux and rotor speed. In the proposed control scheme, the sliding mode observer is improved to achieve the rotor speed and rotor flux identification under healthy and arbitrary open circuit faults. The stability of the observer is proved by the Lyapunov function. The quasi proportional resonance (QPR) controller is introduced in the harmonic plane to suppress the harmonic current after the fault. The simulation and experiment results show that the proposed sensorless fault-tolerant control strategy based on sliding mode observer can accurately and effectively identify the rotor speed and rotor flux of the machine under normal and fault conditions.

INDEX TERMS Multiphase induction machine, fault-tolerant, speed sensorless, sliding mode observer (SMO).

NOMENCLATURE

K	Sliding mode gain
R_s, R_r	Stator, rotor resistance
T	Coordinate transformation matrix
$\Delta\theta_r$	Compensate amount rotor position angle
$\boldsymbol{L}_{sr}, \boldsymbol{L}_{rs}$	Stator and rotor mutual inductance matrix
$\boldsymbol{L}_{ss}, \boldsymbol{L}_{rr}$	Stator and rotor self inductance matrix
$\boldsymbol{I}_s, \boldsymbol{I}_r$	Stator, rotor current vector
$\boldsymbol{U}_s, \boldsymbol{U}_r$	Stator, rotor voltage vector
η	Reciprocal of rotor time constant
$\lambda_{r\alpha}, \lambda_{r\beta}$	Replacement amount of sliding mode function
$\lambda_{r\alpha}^{eq}, \lambda_{r\beta}^{eq}$	Filtered equivalent of $\lambda_{r\alpha}, \lambda_{r\beta}$
ω_1	Synchronous angular velocity
ω_r	Rotor angular velocity
ω_{cf}	Cut-off frequency of low pass filter
ω_c	Cut-off frequency of PR regulator
$\psi_{r\alpha}, \psi_{r\beta}$	Rotor flux of α, β axis
$\psi_{s\alpha}, \psi_{s\beta}$	Stator flux of α, β axis
τ_r	Rotor time constant
θ_r	Rotor position angle
$i_{r\alpha}, i_{r\beta}$	Rotor current of α, β axis
$i_{s\alpha}, i_{s\beta}$	Stator current of α, β axis
p	Differential operator
$u_{r\alpha}, u_{r\beta}$	Rotor voltage of α, β axis
$u_{s\alpha}, u_{s\beta}$	Stator voltage of α, β axis
$\bar{X}$	Estimated error of variable X
$\hat{X}$	Estimated value of variable X
V	Lyapunov function

The associate editor coordinating the review of this manuscript and approving it for publication was Xiaodong Sun.

I. INTRODUCTION

In the multiphase machine drive system, due to the increase of phase number, the redundancy ability of the machine system is improved. More than 70% of motor drive system faults will eventually appear as open-phases fault or switch devices invalidity [1]. When stator phase failure occurs, the corresponding fault tolerant control strategy can be implemented to keep the air gap flux to be constant, so that the machine will continue to run smoothly, and the reliability of the system can be increased greatly. Therefore, the multiphase machine drive

2169-3536 © 2019 IEEE. Translations and content mining are permitted for academic research only.
Personal use is also permitted, but republication/redistribution requires IEEE permission.
See http://www.ieee.org/publications_standards/publications/rights/index.html for more information.

system has been widely used in electric vehicles, rail traffic, ship propulsion and other occasions.

When the motor is unbalanced, the asymmetry of the power supply will cause a large pulsation of the motor output torque. Therefore, the key of fault-tolerant control is to compensate the asymmetry of the magnetomotive force in the air gap to suppress torque ripple. Fault-tolerant control strategies for multiphase motors can be roughly divided into three types: field-oriented control, direct torque control and optimal current control based on open-phase decoupling mathematical model. The first control method was suggested by Y.Zhao [2], [3], and the basic idea is that according to the situation of open-phases, the mathematical model of the unbalanced state is established through the space decoupling transformation and asymmetric rotation transformation after open-phases fault. Finally, the field orientation control under unbalanced state is established.

Direct torque control(DTC) strategy based on open-phase decoupling model is to re-divide the sector by analyzing the post-fault space voltage vectors, and to eliminate harmonic currents as much as possible by reasonably utilizing the vector relationship between $\alpha\beta$-plane and $z_1 - z_2$-plane. Because the stator flux observation is only related to the stator resistance, but unrelated to the inductance parameters of the motor, the sudden change of the inductance parameters of the motor has no effect on the post-fault stator flux observation, so the robustness is strong. The space voltage vector of a five-phase induction motor under one-phase opened is analyzed in [4]. By using the relationship between space voltage vectors, the post-fault direct torque control is realized. In [5], a model reference adaptive system (MRAS) estimator based on the second-order sliding-mode (SOSM) strategy for speed-sensorless direct torque control (DTC) of a six-phase induction motor is proposed. For six-phase induction motors (SPIM), few literatures have proposed the direct torque control strategy for the post-fault SPIM. Because the post-fault space voltage vector is asymmetrical and the amplitude is not uniform, the traditional direct torque control will produce large torque ripple and current harmonics. For different open-phase cases, the vector and sector are also different. This method is not universal and needs to study more practical methods.

The optimal current fault tolerant control is first proposed by H.A.Toliya [6]. The core idea is that by properly controlling the current of the remaining active phases, the motor can still generate a circular flux linkage after the fault, and obtain a sinusoidal rotational magnetomotive force(MMF), thereby obtaining a smooth motor torque output. At the same time, under the premise of ensuring the circular MMF, each phase current can be optimized. The optimization objective is to minimize the copper consumption [7], the amplitude of each phase current [8] and the torque ripple [9], etc. The key of the optimal current control performance is the control of the current loop, hysteresis loop control, proportional resonance (PR) control and model predictive control (MPC) are widely used in the fault-tolerant current loop [10]–[12].

At present, advanced control strategies such as internal model control [13], [14] and state feedback control [15] have been applied in motor control. The wide research of sensorless technology provides a backup scheme for the system when the speed encoder failure, which improves the reliability of the machine drive system and reduces the economic cost. At present, the sensorless algorithm for multiphase induction machine mainly includes the openloop speed estimation based on the model, the signal injection, and closed-loop observer, whereas the closed-loop observer can be divided into the full order state observer, extended Kalman filter, model reference adaptive observer and SMO, and so on. When SPIM under open-phases fault conditions, with the change of electromagnetic parameters, the traditional observer based on mathematical model cannot identify the speed and flux accurately. The observer must be improved to meet the needs of fault-tolerant operation. Few literatures proposed to estimate the speed of multiphase induction motor under open-phases fault. In [16], a inverse speed observer of a bearingless induction motor drive with the artificial neural network is proposed. In [17], [18], a robust observer is proposed to estimate the speed of SPIM in healthy condition. In [19], robust adaptive backstepping sliding mode control (ABSMC) with recurrent wavelet fuzzy neural network (RWFNN) is proposed for the speed regulation of a six-phase permanent magnet synchronous motor (PMSM) demonstrating parameter perturbations and load disturbances. In [20], the MRAS observer is used to realize the speed estimation of five-phase induction machine in one phase open circuit. However, the change of the machine parameters affects the robustness and accuracy of the speed estimation, which means the inherent shortcomings are still inevitable. In [21], a Luenberger observer is designed to estimate the speed of SPIM under one phase, two phase and three phase faults. A SMO with stator resistance identification is proposed in [22], which realizes the speed estimation of five-phase induction machine. However, the parameter design of adaptive controller is very complex. In [23], a robust sliding mode observer with wide speed range is proposed to realize sensorless fault-tolerant control of five-phase FTFSCW-IPM motor.

In order to solve the above problems, this paper deduces the unified fault mathematical model of six-phase induction machine and inductance coefficients under different faults, and establishes a speed-sensorless fault-tolerant control system for six-phase induction motor. Aiming at the harmonic current in the harmonic plane, proportional resonance controller is adopted to suppress them, and a sliding mode observer is improved to realize the identification of speed and flux after fault. Saturation function, instead of sign function, is used to reduce chattering in sliding mode control. The rotor speed estimation is independent of stator current and rotor flux estimation, and therefore the estimation error of the rotor time constant and rotor speed does not serve as feedback into the system. The robust performance and the reliability of the system is improved. The simulation and

experimental results show the correctness and effectiveness of the improved SMO and fault tolerant control strategy.

II. UNIFIED MATHEMATICAL MODEL AND TORQUE RIPPLE ANALYSIS OF SIX-PHASE INDUCTION MOTOR WITH PHASE-MISSING FAULT

A. UNIFIED MATHEMATICAL MODEL WITH PHASE-MISSING FAULT

The six-phase induction machine consists of two sets of conventional three phase windings, ABC and DEF. Each set of windings is Y-connected, and the angle between the two sets of three-phase windings are γ, there are two types. The first one with 60 electrical degrees phase-shift in between two consecutive phases known as symmetrical SPIM and the other one with 30 electrical degrees phase-shift in between two consecutive phases known as asymmetrical SPIM. When the motor is running under normal condition, the neutral point isolation method is adopted to avoid the zero sequence current, as is shown in Fig. 1(b). However, the non-isolated neutral point can effectively reduce the post-fault stator copper loss and output more torque [24], as is shown in Fig. 1(a).

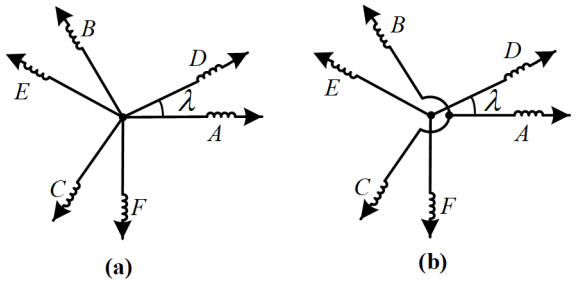

FIGURE 1. Stator winding magnetic axes in an asymmetrical six-phase induction machine with (a) Isolated neutral points (b) Non-isolated neutral points.

The mathematical model of a six-phase induction machine can be decomposed into two subspace, $\alpha\beta$-subspace and z-subspace. The former represents the electromechanical energy conversion subspace while the latter only related to losses. The two-dimensional orthogonal vectors α_0, β_0 of the $\alpha\beta$-subspace can be obtained by (1)

$$\begin{bmatrix}\alpha_0\\ \beta_0\end{bmatrix}=\begin{bmatrix}\cos(\varphi_0+\varphi_1) & \sin(\varphi_0+\varphi_1)\\ \cos(\varphi_0+\varphi_2) & \sin(\varphi_0+\varphi_2)\\ \cos(\varphi_0+\varphi_3) & \sin(\varphi_0+\varphi_3)\\ \cos(\varphi_0+\varphi_4) & \sin(\varphi_0+\varphi_4)\\ \cos(\varphi_0+\varphi_5) & \sin(\varphi_0+\varphi_5)\\ \cos(\varphi_0+\varphi_6) & \sin(\varphi_0+\varphi_6)\end{bmatrix}^T \tag{1}$$

where $\varphi_i(1 \leqslant i \leqslant 6)$ are the stator current phase angles defined as: $\varphi_1 = 0, \varphi_2 = \gamma, \varphi_3 = 2\pi/3, \varphi_4 = 2\pi/3+\gamma, \varphi_5 = 4\pi/3, \varphi_6 = 4\pi/3+\gamma$. φ_0 is the angle between the A axis and α axis. When the machine is healthy, the α axis coincides with the A axis, that is, $\varphi_0 = 0$. When fault occurs, according to the case of the broken phase, the corresponding term of $[\alpha_0\beta_0]^T$ is removed, and the two-dimensional orthogonal vector $\alpha\beta$ is obtained. From the expression of $\alpha\beta^T = 0$, φ_0 can be obtained by (2).

$$\varphi_0 = -\frac{1}{2}\tan^{-1}\left(\frac{\sum_j \sin(2\varphi_j)}{\sum_j cos(2\varphi_j)}\right) \tag{2}$$

It can be deduced that φ_0 is the angle between the α and A axes. φ_j is the phase angle of the remaining effective phase. For example, when 'F' phase is opened (j = 1 to 5) and $\gamma = \pi/2$, the (2) gives $\varphi_0 = 0$ and then, $[\alpha\beta]^T$ become (3).

$$\begin{bmatrix}\alpha\\ \beta\end{bmatrix}=\begin{bmatrix}\cos 0 & \cos\sigma & \cos 4\sigma & \cos 5\sigma & \cos 8\sigma\\ \sin 0 & \sin\sigma & \sin 4\sigma & \sin 5\sigma & \sin 8\sigma\end{bmatrix} \tag{3}$$

where $\sigma = \pi/6$.

The electromechanical energy conversion takes place only in $\alpha\beta$-subspace which means that the MMF produced by active phases is equivalent to the MMF produced by two windings on the axes α and β with the currents$i_{s\alpha}$ and $i_{s\beta}$, respectively. These currents are defined by (4)

$$\begin{bmatrix}i_{s\alpha}\\ i_{s\beta}\end{bmatrix} = [\boldsymbol{T}_c]\,[\boldsymbol{I}_s] \tag{4}$$

where

$$[\boldsymbol{T}_c] = \begin{bmatrix}[\alpha]/\,\|\alpha\|\\ [\beta]/\,\|\beta\|\end{bmatrix} \tag{5}$$

In (5), $\|\alpha\|$ and $\|\beta\|$ are vector norms of $\alpha\beta$-subplanes respectively. The z-subspace is defined by N-2 orthonormal basis vectors (three vectors $[z_1]$, $[z_2]$ and $[z_3]$ for N = 5) and it has to be orthogonal to $\alpha\beta$-subspace [2]. On the other hand, $[z_1]-[z_2]-[z_3]$ give the basis of the null space of $[\boldsymbol{T}_c]$, as is shown in (6).

$$[\boldsymbol{T}_z] = null([\boldsymbol{T}_c]^T) = \begin{bmatrix}[z_1]/\,\|z_1\|\\ [z_2]/\,\|z_2\|\\ [z_3]/\,\|z_3\|\end{bmatrix} \tag{6}$$

According to $[\boldsymbol{T}_z]$ and $[\boldsymbol{T}_c]$, the decoupling transformation matrix $[\boldsymbol{T}_N]$ can be obtained, as is shown in (7).

$$[\boldsymbol{T}_N] = \begin{bmatrix}[\boldsymbol{T}_c]\\ [\boldsymbol{T}_z]\end{bmatrix} \tag{7}$$

The space decoupling transformation matrix $[\boldsymbol{T}_N]$ is substituted into the stator and rotor voltage equation, as is shown in (8).

$$\begin{cases}\boldsymbol{T}_N\boldsymbol{U}_s = \boldsymbol{T}_N R_s \boldsymbol{T}_N^{-1}\boldsymbol{T}_N\boldsymbol{I}_s\\ \qquad\qquad +p(\boldsymbol{T}_N L_{ss}\boldsymbol{T}_N^{-1}\boldsymbol{T}_N\boldsymbol{I}_s + \boldsymbol{T}_N L_{sr}\boldsymbol{T}_6^{-1}\boldsymbol{T}_6\boldsymbol{I}_r)\\ \boldsymbol{T}_6\boldsymbol{U}_r = \boldsymbol{T}_6 R_r \boldsymbol{T}_6^{-1}\boldsymbol{T}_6\boldsymbol{I}_r\\ \qquad\qquad +p(\boldsymbol{T}_6 L_{rr}\boldsymbol{T}_6^{-1}\boldsymbol{T}_6\boldsymbol{I}_r + \boldsymbol{T}_6 L_{rs}\boldsymbol{T}_N^{-1}\boldsymbol{T}_N\boldsymbol{I}_s)\end{cases} \tag{8}$$

$\boldsymbol{U}_s$ and $\boldsymbol{U}_r$ are residual stator and rotor voltage vectors, $\boldsymbol{I}_s$ and $\boldsymbol{I}_r$ are residual stator and rotor current vectors respectively. R_s and R_r are residual stator and rotor resistance respectively. L_{ss} and L_{rr} are residual stator and rotor self inductance matrix respectively. L_{sr} and L_{rs} are residual stator and rotor mutual inductance matrix respectively. $\boldsymbol{T}_6$ is

the original space decoupling transformation matrix, which will be given at the following article. An unified stator and rotor voltage equations of a six-phase induction machine under open phase fault conditions in the $\alpha\beta$-subspace, as is shown in (9).

$$\begin{cases} \begin{bmatrix} u_{s\alpha} \\ u_{s\beta} \end{bmatrix} = \begin{bmatrix} R_s & 0 \\ 0 & R_s \end{bmatrix} \begin{bmatrix} i_{s\alpha} \\ i_{s\beta} \end{bmatrix} + p \left\{ \begin{bmatrix} L_{s\alpha} & 0 \\ 0 & L_{s\beta} \end{bmatrix} \begin{bmatrix} i_{s\alpha} \\ i_{s\beta} \end{bmatrix} \right\} \\ + p \left\{ \begin{bmatrix} L_{m\alpha}\cos(\theta_r+\varphi_0) & -L_{m\alpha}\sin(\theta_r+\varphi_0 \\ L_{m\beta}\sin(\theta_r+\varphi_0) & L_{m\beta}\cos(\theta_r+\varphi_0) \end{bmatrix} \begin{bmatrix} i_{r\alpha} \\ i_{r\beta} \end{bmatrix} \right\} \\ \begin{bmatrix} u_{r\alpha} \\ u_{r\beta} \end{bmatrix} = \begin{bmatrix} R_r & 0 \\ 0 & R_r \end{bmatrix} \begin{bmatrix} i_{r\alpha} \\ i_{r\beta} \end{bmatrix} + p \left\{ \begin{bmatrix} Lr & 0 \\ 0 & Lr \end{bmatrix} \begin{bmatrix} i_{r\alpha} \\ i_{r\beta} \end{bmatrix} \right\} \\ + p \left\{ \begin{bmatrix} L_{m\alpha}\cos(\theta_r+\varphi_0) & L_{m\beta}\sin(\theta_r+\varphi_0) \\ -L_{m\alpha}\sin(\theta_r+\varphi_0) & L_{m\beta}\cos(\theta_r+\varphi_0) \end{bmatrix} \begin{bmatrix} i_{s\alpha} \\ i_{s\beta} \end{bmatrix} \right\} \end{cases} \tag{9}$$

where L_r is rotor inductance,$L_{m\alpha}$, $L_{m\beta}$,$L_{s\alpha}$ and $L_{s\beta}$ are stator and rotor mutual inductance and the stator self inductance under the two-phase stationary coordinate system respectively. θ_r is the rotor position angle, and p is the differential operator. Using the rotation transformation matrix $\boldsymbol{T}_r$, as shown in the (10).

$$\boldsymbol{T}_r = \begin{bmatrix} \cos(\theta_r+\varphi_0) & -\sin(\theta_r+\varphi_0) \\ \sin(\theta_r+\varphi_0) & \cos(\theta_r+\varphi_0) \end{bmatrix} \tag{10}$$

The left side of the rotor current term in the stator voltage equation in (9) is multiplied by matrix $\boldsymbol{T}_r^{-1}\boldsymbol{T}_r$, and the rotor voltage equation is multiplied by matrix $\boldsymbol{T}_r$ on the left side, which realizes that the rotor side variables in stator and rotor voltage equations are transformed into static coordinate system of the stator side. An unified mathematical model of open-phases faults is established in the $\alpha\beta$-subspace. The stator and rotor voltage equation are expressed as

$$\begin{cases} \begin{bmatrix} u_{s\alpha} \\ u_{s\beta} \end{bmatrix} = R_s \begin{bmatrix} i_{s\alpha} \\ i_{s\beta} \end{bmatrix} + p \begin{bmatrix} \psi_{s\alpha} \\ \psi_{s\beta} \end{bmatrix} \\ \begin{bmatrix} u_{r\alpha} \\ u_{r\beta} \end{bmatrix} = R_r \begin{bmatrix} i_{r\alpha} \\ i_{r\beta} \end{bmatrix} + p \begin{bmatrix} \psi_{r\alpha} \\ \psi_{r\beta} \end{bmatrix} + \begin{bmatrix} 0 & \omega_r \\ -\omega_r & 0 \end{bmatrix} \begin{bmatrix} \psi_{r\alpha} \\ \psi_{r\beta} \end{bmatrix} \end{cases} \tag{11}$$

The stator and rotor flux are expressed as

$$\begin{cases} \begin{bmatrix} \psi_{s\alpha} \\ \psi_{s\beta} \end{bmatrix} = \begin{bmatrix} L_{s\alpha} & 0 \\ 0 & L_{s\beta} \end{bmatrix} \begin{bmatrix} i_{s\alpha} \\ i_{s\beta} \end{bmatrix} + \begin{bmatrix} L_{m\alpha} & 0 \\ 0 & L_{m\beta} \end{bmatrix} \begin{bmatrix} i_{r\alpha} \\ i_{r\beta} \end{bmatrix} \\ \begin{bmatrix} \psi_{r\alpha} \\ \psi_{r\beta} \end{bmatrix} = L_r \begin{bmatrix} i_{r\alpha} \\ i_{r\beta} \end{bmatrix} + \begin{bmatrix} L_{m\alpha} & 0 \\ 0 & L_{m\beta} \end{bmatrix} \begin{bmatrix} i_{s\alpha} \\ i_{s\beta} \end{bmatrix} \end{cases} \tag{12}$$

where $\psi_{s\alpha}$, $\psi_{s\beta}$, $\psi_{r\alpha}$ and $\psi_{r\beta}$ are the components of the stator and rotor flux respectively. The stator voltage equations in z-subspace are described as

$$\begin{bmatrix} u_{z1} \\ u_{z2} \\ u_{z3} \end{bmatrix} = \begin{bmatrix} R_s + L_{ls} \cdot p & 0 & 0 \\ 0 & R_s + L_{ls} \cdot p & 0 \\ 0 & 0 & R_s + L_{ls} \cdot p \end{bmatrix} \begin{bmatrix} i_{z1} \\ i_{z2} \\ i_{z3} \end{bmatrix} \tag{13}$$

Equations (11) and (12) show that the model in $\alpha\beta$-subspace with an asymmetric winding under open-phases faults, the voltage equation in the z-subspace is only related to the R_s and L_{ls}, but not related to the condition of open-phased fault. For different situations, the value of $L_{s\alpha}$, $L_{s\beta}$, $L_{m\alpha}$ and $L_{m\beta}$ are different, and the expression of the electromagnetic torque is described as

$$T_e = p_n(L_{m\beta} i_{s\beta} i_{r\alpha} - L_{m\alpha} i_{s\alpha} i_{r\beta}) \tag{14}$$

where p_n is the number of pole-pairs.

The winding structure of six-phase induchine machine under normal and three different kinds of phase-missing conditions are shown in Fig. 2. In this paper, the sensorless field oriented control under normal and three kinds of phase-missing faults will be deeply studied respectively.

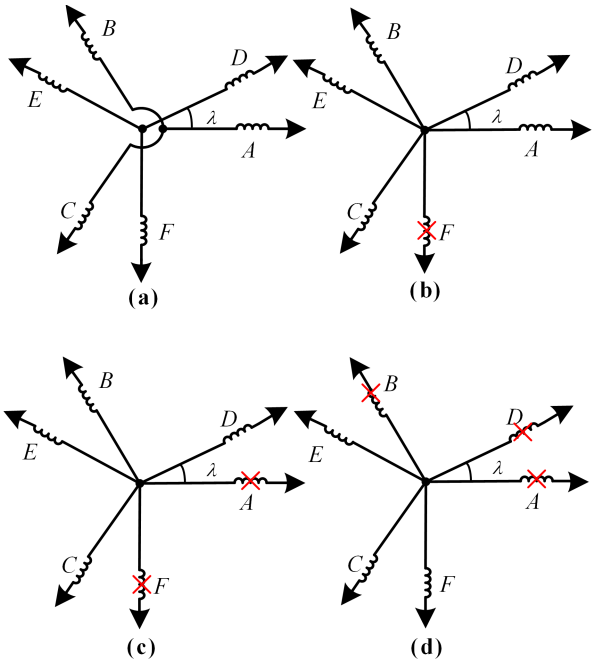

FIGURE 2. Phase missing situation. (a) Healthy. (b) F phase missing. (c) A and F phase missing. (d) A, B and D phase missing.

According to the principle of energy conversion, the space decoupling transformation matrix of three kinds of phase-missing faults can be derived from the above method. For normal and fault cases (four cases shown in Fig. 2, the original transformation matrix is $\boldsymbol{T}_6$, the decoupling matrices in the other three cases are $\boldsymbol{T}_5$, $\boldsymbol{T}_4$ and $\boldsymbol{T}_3$ respectively, as is

TABLE 1. Machine inductances with open phase(s) for $\gamma = \frac{\pi}{6}$.

Faulted phases	$L_{s\alpha}$	$L_{s\beta}$	$L_{m\alpha}$	$L_{m\beta}$
A;D;E	L_{ls}+2L_{ms}	$L_{ls}+3L_{ms}$	$2.449L_{ms}$	$3L_{ms}$
B;C;F	$L_{ls}+3L_{ms}$	$L_{ls}+2_{L}ms$	$3L_{ms}$	$2.449L_{ms}$
(A,D);(A,E);(D,C);(B,E)	$L_{ls}+1.134L_{ms}$	$L_{ls}+2.866L_{ms}$	$1.844L_{ms}$	$2.932L_{ms}$
(A,B);(A,C);(D,E)	$L_{ls}+1.5L_{ms}$	$L_{ls}+2.5L_{ms}$	$2.1213L_{ms}$	$2.7386L_{ms}$
(A,F);(D,B);(E,C)	$L_{ls}+2L_{ms}$	$L_{ls}+2L_{ms}$	$2.449L_{ms}$	$2.449L_{ms}$
(D,F);(B,C);(E,F)	$L_{ls}+2.5L_{ms}$	$L_{ls}+1.5L_{ms}$	$2.7386L_{ms}$	$2.1213L_{ms}$
(B,F);(C,F)	$L_{ls}+2.866L_{ms}$	$L_{ls}+1.134L_{ms}$	$2.932L_{ms}$	$1.844L_{ms}$
(A,D,B);(A,D,F);(D,B,E,) (A,E,C,);(A,E,F);(D,E,C,)	$L_{ls}+L_{ms}$	$L_{ls}+2L_{ms}$	$1.7321L_{ms}$	$2.449L_{ms}$
(A,D,E);(A,D,C);(A,B,E)	$L_{ls}+0.5L_{ms}$	$L_{ls}+2.5L_{ms}$	$1.2247L_{ms}$	$2.7386L_{ms}$
(D,B,C);(D,B,F);(B,E,C) (E,C,F);(A,B,F);(A,C,F)	$L_{ls}+2L_{ms}$	$L_{ls}+L_{ms}$	$2.449L_{ms}$	$1.7321L_{ms}$
(B,E,F);(D,C,F);(B,C,F)	$L_{ls}+2.5L_{ms}$	$L_{ls}+0.5L_{ms}$	$2.7386L_{ms}$	$1.2247L_{ms}$
(A,B,C);(D,E,F)	$L_{ls}+1.5L_{ms}$	$L_{ls}+1.5L_{ms}$	$2.1213L_{ms}$	$2.1213L_{ms}$

shown in (15) - (18).

$$\boldsymbol{T}_6 = \frac{1}{\sqrt{3}}\begin{bmatrix} 1 & \frac{\sqrt{3}}{2} & -\frac{1}{2} & -\frac{\sqrt{3}}{2} & -\frac{1}{2} & 0 \\ 0 & \frac{1}{2} & \frac{\sqrt{3}}{2} & \frac{1}{2} & -\frac{\sqrt{3}}{2} & -1 \\ 1 & -\frac{\sqrt{3}}{2} & -\frac{1}{2} & \frac{\sqrt{3}}{2} & -\frac{1}{2} & 0 \\ 0 & \frac{1}{2} & -\frac{\sqrt{3}}{2} & \frac{1}{2} & \frac{\sqrt{3}}{2} & -1 \\ 1 & 0 & 1 & 0 & 1 & 0 \\ 0 & 1 & 0 & 1 & 0 & 1 \end{bmatrix} \tag{15}$$

$$\boldsymbol{T}_5 = \frac{1}{\sqrt{3}}\begin{bmatrix} 1 & \frac{\sqrt{3}}{2} & -\frac{1}{2} & -\frac{\sqrt{3}}{2} & -\frac{1}{2} \\ 0 & \frac{\sqrt{6}}{4} & \frac{3\sqrt{2}}{4} & \frac{\sqrt{6}}{4} & -\frac{3\sqrt{2}}{4} \\ 1 & -\frac{\sqrt{3}}{2} & -\frac{1}{2} & \frac{\sqrt{3}}{2} & -\frac{1}{2} \\ 0 & \frac{3\sqrt{2}}{4} & -\frac{\sqrt{6}}{4} & \frac{3\sqrt{2}}{4} & \frac{\sqrt{6}}{4} \\ 1 & 0 & 1 & 0 & 1 \end{bmatrix} \tag{16}$$

$$\boldsymbol{T}_4 = \frac{\sqrt{2}}{4}\begin{bmatrix} \sqrt{3} & -1 & -\sqrt{3} & -1 \\ 1 & \sqrt{3} & 1 & -\sqrt{3} \\ 0 & -2 & \sqrt{3} & -1 \\ 2 & 0 & 1 & \sqrt{3} \end{bmatrix} \tag{17}$$

$$\boldsymbol{T}_3 = \begin{bmatrix} -\frac{\sqrt{3}}{2} & -\frac{1}{2} & 0 \\ \frac{\sqrt{2}}{4} & -\frac{\sqrt{6}}{4} & -\frac{\sqrt{2}}{2} \\ \frac{\sqrt{2}}{4} & -\frac{\sqrt{6}}{4} & \frac{\sqrt{2}}{2} \end{bmatrix} \tag{18}$$

The above space decoupling matrices are substituted into (8) respectively, and through the rotor side variable transformation to the stator side, the inductance parameters can be obtained under three kinds of fault conditions. According to this method, the inductance parameters can be obtained under any fault conditions, as shown in Table 1, the parameters of the symmetrical SPIM have been given in [8].

B. TORQUE RIPPLE ANALYSIS

From (12), The post-fault flux equation of $\alpha\beta$-subspace can be obtained as

$$\begin{cases} \dfrac{d\psi_{r\alpha}}{dt} = -\dfrac{1}{T_r}\psi_{r\alpha} - \omega_r\psi_{r\beta} + \dfrac{L_{m\alpha}}{T_r}i_{s\alpha} \\ \dfrac{d\psi_{r\beta}}{dt} = -\dfrac{1}{T_r}\psi_{r\beta} + \omega_r\psi_{r\alpha} + \dfrac{L_{m\beta}}{T_r}i_{s\beta} \end{cases} \tag{19}$$

where, ω_r is the rotor angular speed. Assume that

$$\begin{cases} i_{s\alpha} = I_\alpha \cos\omega_1 t \\ i_{s\beta} = I_\beta \sin\omega_1 t \end{cases} \tag{20}$$

Substituting (20) into (19) yields

$$\begin{cases} \psi_{r\alpha} = \dfrac{1}{D}\Big[\tau_r\omega_r L_{m\beta} I_\beta \cos(\omega_1 t - \phi_1) \\ \qquad +\sqrt{1+\tau_r^2\omega_1^2}L_{m\alpha}I_\alpha \sin(\omega_1 t - \phi_1 + \phi_2)\Big] \\ \psi_{r\beta} = \dfrac{1}{D}\Big[\tau_r\omega_r L_{m\alpha} I_\alpha \sin(\omega_1 t - \phi_1) \\ \qquad -\sqrt{1+\tau_r^2\omega_1^2}L_{m\beta}I_\beta \cos(\omega_1 t - \phi_1 + \phi_2)\Big] \end{cases} \tag{21}$$

where, $D = \sqrt{[1+\tau_r^2(\omega_r^2-\omega_1^2)]^2 + 4\tau_r^2\omega_1^2}$, $\phi_1 = tan^{-1}[(2\tau_r\omega_1)/(1+\tau_r^2\omega_r^2-\tau_r^2\omega_1^2)]$, $\phi_2 = tan^{-1}(\tau_r\omega_1)$, τ_r is the rotor time constant, ω_1 is the synchronous angular velocity.

The electromagnetic torque can be divided into two parts, the first part $\bar{T}_e$ is a constant component and the second part

$\tilde{T}_e$ is an alternating component, as is shown in (22).

$$T_e = p_n(L_{m\beta} i_{s\beta} i_{r\alpha} - L_{m\alpha} i_{s\alpha} i_{r\beta}) = \bar{T}_e + \tilde{T}_e \tag{22}$$

The constant component $\bar{T}$ can be expressed as

$$\bar{T}_e = \frac{p_n}{DL_r}\left[L_{m\alpha}L_{m\beta}I_\alpha I_\beta\sqrt{1+\tau_r^2\omega_1^2}\sin(\phi_1-\phi_2) - \frac{\tau_r\omega_r}{2}(L_{m\alpha}^2 I_\alpha^2 + L_{m\beta}^2 I_\beta^2)\cos(\varphi_1)\right] \tag{23}$$

The alternating component $\tilde{T}$ can be expressed as

$$\tilde{T}_e = \frac{p_n}{2DL_r}\tau_r\omega_r(L_{m\alpha}^2 I_\alpha^2 - L_{m\beta}^2 I_\beta^2)\cos(2\omega_1 t - \phi_1) \tag{24}$$

From (24), in order to eliminate the torque ripple after the motor failure, the following constraints are required.

$$L_{m\alpha}^2 I_\alpha^2 - L_{m\beta}^2 I_\beta^2 = 0 \tag{25}$$

The above conditions can be equivalent to

$$\left|\frac{I_\alpha}{I_\beta}\right| = \frac{L_{m\beta}}{L_{m\alpha}} = \frac{\|\beta\|}{\|\alpha\|} \tag{26}$$

From (24)-(26), after the fault, the frequency of the torque ripple is twice the fundamental frequency, and the suppression of the torque ripple can be achieved by controlling the amplitude of the stator current of the $\alpha\beta$-subspace.

III. FIELD ORIENTED CONTROL OF SIX-PHASE INDUCTION MACHINE UNDER OPEN-PHASE FAULT

A. FIELD ORIENTATION CONTROL IN $\alpha\beta$-SUBSPACE UNDER OPEN-PHASE FAULT

Due to the asymmetry of the stator windings on the axes α and β, in order to get the same equation as the symmetrical winding structure and minimize torque oscillation, the new rotation transformation matrix is $T_{2s/2r}^e$ [2], as is shown in (27).

$$T_{2s/2r}^e = \begin{bmatrix} k_\beta\cos\theta_r & k_\alpha\sin\theta_r \\ -k_\beta\sin\theta_r & k_\alpha\cos\theta_r \end{bmatrix} \tag{27}$$

where, the values of k_α and k_β are

$$\frac{k_\alpha}{k_\beta} = \frac{L_{m\beta}}{L_{m\alpha}} = \frac{\|\beta\|}{\|\alpha\|} \tag{28}$$

Substitution from (28) into (27) gives

$$T_{2s/2r}^e = \begin{bmatrix} \sqrt{\frac{L_{m\alpha}}{L_{m\beta}}}\cos\theta_r & \sqrt{\frac{L_{m\beta}}{L_{m\alpha}}}\sin\theta_r \\ -\sqrt{\frac{L_{m\alpha}}{L_{m\beta}}}\sin\theta_r & \sqrt{\frac{L_{m\beta}}{L_{m\alpha}}}\cos\theta_r \end{bmatrix} \tag{29}$$

When the machine structure is balanced, $L_{m\alpha} = L_{m\beta}$, and then, the rotation transformation matrix $T_{2s/2r}^e$ transformed into its original state.

The rotor winding is symmetrical, and its rotation transformation matrix is symmetrical as well. After multiplying unbalanced and balanced transformation matrices respectively in the variables of the stator side and rotor side, the voltage equation and flux equation of stator and rotor in the dq coordinate system are obtained, as is shown in (30).

$$\begin{cases} U_{sdq} = R_s I_{sdq} + \dfrac{d\left[\psi_{sdq}\right]}{dt} + \begin{bmatrix} 0 & -\omega_1 \\ \omega_1 & 0 \end{bmatrix}\left[\psi_{rdq}\right] \\ U_{rdq} = R_r I_{rdq} + \dfrac{d\left[\psi_{rdq}\right]}{dt} + \begin{bmatrix} 0 & -(\omega_1-\omega_r) \\ (\omega_1-\omega_r) & 0 \end{bmatrix}\left[\psi_{rdq}\right] \\ \begin{bmatrix} \psi_{sdq} \\ \psi_{rdq} \end{bmatrix} = \begin{bmatrix} \left[L_{ss}^{dq}\right] & \left[L_{sr}^{dq}\right] \\ \left[L_{rs}^{dq}\right] & \left[L_{rr}^{dq}\right] \end{bmatrix}\begin{bmatrix} I_{sdq} \\ I_{rdq} \end{bmatrix} \end{cases} \tag{30}$$

where, L_{rr}^{dq} and L_{rs}^{dq} are the inductance matrix in rotor flux equation and are expressed as

$$\begin{cases} L_{rr}^{dq} = \begin{bmatrix} L_r & 0 \\ 0 & L_r \end{bmatrix} \\ L_{rs}^{dq} = \begin{bmatrix} \sqrt{L_{m\alpha}L_{m\beta}} & 0 \\ 0 & \sqrt{L_{m\alpha}L_{m\beta}} \end{bmatrix} \end{cases} \tag{31}$$

The inductance matrix in stator flux equation L_{ss}^{dq} and L_{sr}^{dq} as

$$\begin{cases} L_{ss}^{dq} = \begin{bmatrix} \sigma_1 & \sigma_2 \end{bmatrix} \\ L_{sr}^{dq} = \begin{bmatrix} \sigma_3 & \sigma_4 \end{bmatrix} \end{cases} \tag{32}$$

where

$$\sigma_1 = \begin{bmatrix} \frac{L_{s\alpha}+L_{s\beta}}{2} + \frac{L_{s\alpha}-L_{s\beta}}{2}\cos(2\theta_r) \\ -\frac{L_{s\alpha}-L_{s\beta}}{2}\sin(2\theta_r) \end{bmatrix}$$

$$\sigma_2 = \begin{bmatrix} -\frac{L_{s\alpha}-L_{s\beta}}{2}\sin(2\theta_r) \\ \frac{L_{s\alpha}+L_{s\beta}}{2} - \frac{L_{s\alpha}-L_{s\beta}}{2}\cos(2\theta_r) \end{bmatrix}$$

$$\sigma_3 = \begin{bmatrix} \frac{L_{m\alpha}^2+L_{m\beta}^2}{2\sqrt{L_{m\alpha}L_{m\beta}}} + \frac{L_{m\alpha}^2-L_{m\beta}^2}{2\sqrt{L_{m\alpha}L_{m\beta}}}\cos(2\theta_r) \\ -\frac{L_{m\alpha}^2-L_{m\beta}^2}{2\sqrt{L_{m\alpha}L_{m\beta}}}\sin(2\theta_r) \end{bmatrix}$$

$$\sigma_4 = \begin{bmatrix} -\frac{L_{m\alpha}^2-L_{m\beta}^2}{2\sqrt{L_{m\alpha}L_{m\beta}}}\sin(2\theta_r) \\ \frac{L_{m\alpha}^2+L_{m\beta}^2}{2\sqrt{L_{m\alpha}L_{m\beta}}} + \frac{L_{m\alpha}^2-L_{m\beta}^2}{2\sqrt{L_{m\alpha}L_{m\beta}}}\cos(2\theta_r) \end{bmatrix}$$

The (32) shows that the stator flux is not decoupled in the dq coordinate system. The stator self-inductance and stator-rotor mutual inductance of the dq axis are both related to θ_r, while the rotor flux of the dq axis is decoupled in two directions, so the current component of the dq axis can be decoupled according to the control method of rotor flux orientation.

In the synchronous rotating coordinate system, the torque equation is

$$T_e = \frac{p_n\sqrt{L_{m\alpha}L_{m\beta}}}{L_r}(i_{sq}\psi_{rd} - i_{sd}\psi_{rq}) \tag{33}$$

According to the principle of field oriented control, the direction of the rotor flux is defined to coincide with the d axis, that is, the q axis component is zero, while the d axis component is equal to the magnitude of the flux, as is shown in (34)

$$\begin{cases} \psi_{rq} = 0, \dfrac{d\psi_{rq}}{dt} = 0 \\ \psi_{rd} = \psi_r \end{cases} \tag{34}$$

The rotor flux equation and torque equation after rotor flux orientation can be obtained as

$$\left.\begin{cases} \omega_1 - \omega_r = \omega_s = \dfrac{R_r}{L_r}\dfrac{\sqrt{L_{m\alpha}L_{m\beta}}}{\psi_r} i_{sq} \\ \psi_r = \dfrac{R_r\sqrt{L_{m\alpha}L_{m\beta}}}{L_r p + R_r} i_{sd} \\ T_e = \dfrac{p_n}{L_r}\sqrt{L_{m\alpha}L_{m\beta}} i_{sq}\psi_r \end{cases}\right\} \Rightarrow \theta_r = \int \omega_1 dt \tag{35}$$

Equation (35) shows that the rotor flux is only generated by the excitation component i_{sd} of the stator current, and has nothing to do with the torque component i_{sq}. Therefore, the decoupling of the stator current excitation component and the torque component is realized on the dq rotating coordinates, and the decoupling vector control of the six-phase induction machine is realized when the structure is not balanced. The reference voltage component in the $\alpha\beta$-plane is obtained by this method.

B. PR CONTROL IN HARMONIC SUBSPACE UNDER OPEN-PHASE FAULT

PI controller has good tracking effect on DC component, but poor tracking effect on AC component. Because the current signal in harmonic plane is actually AC, this paper introduces quasi proportional resonance (QPR) control in harmonic plane to suppress the current in harmonic plane after phase absence. QPR regulator has the same proportion with PI regulator, but the integral part is different, so the transfer function can be shown as

$$u_z^* = \left[k_{pi} + k_{ri}\frac{2\omega_c s}{s^2 + 2\omega_c s + \omega_1^2}\right](i_z^* - i_z) \tag{36}$$

where, u_z^* is the given value of harmonic plane voltage, i_z^* and i_z are the given value and feedback value of harmonic plane current respectively. k_{pi} and k_{ri} are proportional and harmonic coefficients of PR controller respectively. ω_1 is the resonant frequency, ω_c is the cut-off frequency and s is the Laplace operator.

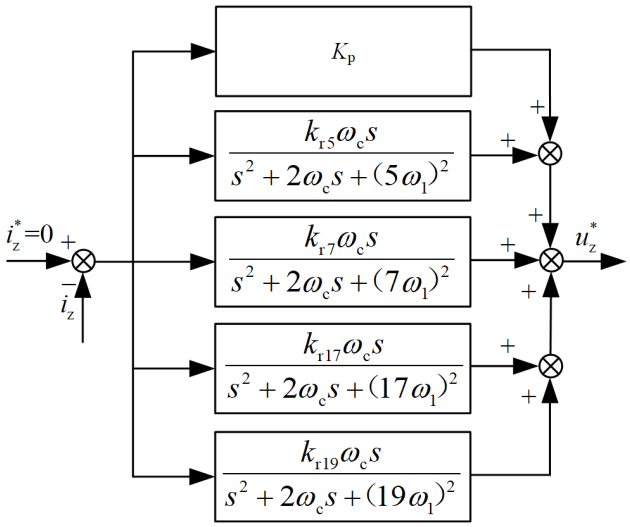

FIGURE 3. PR regulator in harmonic plane.

From the space decoupling matrix of normal and open phase, it can be seen that the $6m \pm 1(m{=}1,3\ldots)$ th harmonic current is projected to the harmonic plane. Therefore, this paper mainly suppresses the 5th, 7th, 17th and 19th harmonics. Fig. 3 shows the structure block diagram of the harmonic plane PR regulator. The output voltage is the superposition of one proportional link and four resonant links. In normal operation, only two harmonic planes are needed because the harmonic plane has only $z_1 - z_2$ plane, and corresponding to different open circuit faults, the number of required regulators are 0-3.

IV. OBSERVER DESIGN METHODOLOGY

A. CURRENT OBSERVER DESIGN

Based on the unified mathematical model of the $\alpha\beta$-subspace under open-phases faults, the state equation is shown in (37).

$$p\begin{bmatrix}\psi_{r\alpha\beta}\\ i_{s\alpha\beta}\end{bmatrix} = \begin{bmatrix}A_{11} & A_{12}\\ A_{21} & A_{22}\end{bmatrix}\begin{bmatrix}\psi_{r\alpha\beta}\\ i_{s\alpha\beta}\end{bmatrix} + \begin{bmatrix}0\\ B\end{bmatrix}\begin{bmatrix}u_{\alpha\beta}\end{bmatrix} \tag{37}$$

where A_{11}, A_{12}, A_{21}, A_{22} and B in (37) are the parameter matrices, as is shown below.

$$A_{11} = -\begin{bmatrix}\dfrac{R_r}{L_r} & \omega_r\\ -\omega_r & \dfrac{R_r}{L_r}\end{bmatrix} \quad A_{12} = \begin{bmatrix}\dfrac{R_r L_{m\alpha}}{L_r} & 0\\ 0 & \dfrac{R_r L_{m\beta}}{L_r}\end{bmatrix}$$

$$A_{21} = -\begin{bmatrix}\dfrac{L_{m\alpha}}{\sigma_1 L_{s\alpha} L_r} & 0\\ 0 & \dfrac{L_{m\beta}}{\sigma_2 L_{s\beta} L_r}\end{bmatrix} A_{11}$$

$$A_{22}=-\begin{bmatrix}\frac{L_{m\alpha}}{\sigma_1 L_{s\alpha}L_r} & 0\\ 0 & \frac{L_{m\beta}}{\sigma_2 L_{s\beta}L_r}\end{bmatrix}A_{12}+\begin{bmatrix}\frac{R_s}{\sigma_1 L_{s\alpha}} & 0\\ 0 & \frac{R_s}{\sigma_2 L_{s\beta}}\end{bmatrix}$$

$$B=\begin{bmatrix}\frac{1}{\sigma_1 L_{s\alpha}} & 0\\ 0 & \frac{1}{(\sigma_2 L_{s\beta})}\end{bmatrix}$$

where, $\sigma_1=1-\frac{L_{m\alpha}^2}{L_{s\alpha}L_r}$, $\sigma_2=1-\frac{L_{m\beta}^2}{L_{s\beta}L_r}$.

In (37), the first term in the stator current equation is the same as the rotor flux linkage equation. That is, the same coupling term exists in the rotor flux and the stator current equation. According to the relationship between the flux and the back electromotive force, the mathematical model of equation (29) can be transformed into

$$\begin{cases}\frac{pi_{s\alpha}}{\varepsilon_\alpha}=\frac{L_r}{L_{m\alpha}}(u_\alpha-R_s i_{s\alpha})-e_{r\alpha}\\ \frac{pi_{s\beta}}{\varepsilon_\beta}=\frac{L_r}{L_{m\beta}}(u_\beta-R_s i_{s\beta})-e_{r\beta}\\ p\psi_{r\alpha}=-e_{r\alpha}\\ p\psi_{r\beta}=-e_{r\beta}\end{cases}\tag{38}$$

where, $\varepsilon_\alpha=\frac{L_{m\alpha}}{\sigma_1 L_{s\alpha}L_r}$, $\varepsilon_\beta=\frac{L_{m\beta}}{\sigma_2 L_{s\beta}L_r}$.

In order to match the sample current with the observer estimated current, a sliding mode observer is designed for current observation. According to the theory of sliding mode variable structure control, a sliding mode observer based on saturation function is designed

$$\begin{cases}\frac{pi_{s\alpha}}{\varepsilon_\alpha}=\frac{L_r}{L_{m\alpha}}(u_\alpha-R_s i_{s\alpha})-Ksat(\hat{i}_{s\alpha}-i_{s\alpha})\\ \frac{pi_{s\beta}}{\varepsilon_\beta}=\frac{L_r}{L_{m\beta}}(u_\beta-R_s i_{s\beta})-Ksat(\hat{i}_{s\beta}-i_{s\beta})\end{cases}\tag{39}$$

where, the symbol $\hat{}$ is the corresponding variable observation value. K is the sliding mode gain coefficient, and the magnitude of K is selected according to the actual control system.

The switching function of the traditional sliding mode observer is a symbol function, which will cause chattering. To eliminate chattering in sliding mode control, a continuous saturated piecewise function is used. The saturation function is as shown in equation (40).

$$sat(\hat{i}_{s\alpha\beta}-i_{s\alpha\beta})=\begin{cases}1 & \hat{i}_{s\alpha\beta}-i_{s\alpha\beta}\geq\Delta\\ \frac{\hat{i}_{s\alpha\beta}-i_{s\alpha\beta}}{\Delta} & -\Delta<\hat{i}_{s\alpha\beta}-i_{s\alpha\beta}<\Delta\\ -1 & \hat{i}_{s\alpha\beta}-i_{s\alpha\beta}\leq-\Delta\end{cases}\tag{40}$$

where, Δ is a small positive number that represents the limit of the current error switching point. When the current observation and actual value are larger than the set current error limit, the output value is the saturation value. When the error is less than the set current error limit, which means the state point reaches the switching surface, the output value of *sat* function can change smoothly. The use of a saturation function effectively reduces slip mode chattering. In addition, when the current error switching point Δ is selected differently, the slope of sliding mode function will change. It is necessary to comprehensively consider the actual situation.

The sliding mode function is represented by the functions $\lambda_{r\alpha}$ and $\lambda_{r\beta}$. During the movement of the sliding mode variable structure on the sliding surface, because of frequent switching, a large number of high-frequency components are generated, and the low-pass filter can be used to filter out high-frequency components to achieve equivalent control.

$$\begin{bmatrix}\lambda_{r\alpha}^{eq}\\ \lambda_{r\beta}^{eq}\end{bmatrix}=\frac{1}{\omega_{cf}s+1}\begin{bmatrix}\lambda_{r\alpha}\\ \lambda_{r\beta}\end{bmatrix}\tag{41}$$

where, ω_{cf} is the cut-off frequency of the low pass filter.

According to the equivalent control formula (41), assuming that the current observation value $\hat{i}_{s\alpha}$, $\hat{i}_{s\beta}$ and the actual value $i_{s\alpha}$, $i_{s\beta}$ are equal when the machine reaches the sliding surface. according to the concept of equivalent control, the rotor flux in the static coordinate system can be obtained by the negative integral of the equivalent control quantity, as is shown in (42).

$$\begin{cases}\hat{\psi}_{r\alpha}=\int-\lambda_{\alpha(eq)}\\ \hat{\psi}_{r\beta}=\int-\lambda_{\beta(eq)}\end{cases}\tag{42}$$

The amplitude and phase of the rotor flux can be described as

$$\begin{cases}\hat{\psi}_r=\sqrt{\hat{\psi}_{r\alpha}^2+\hat{\psi}_{r\beta}^2}\\ \theta_r=\Delta\theta_r+\hat{\theta}_r\end{cases}\tag{43}$$

The θ_r can be extended to four quadrants. In order to compensate the phase lag caused by the low pass filter, the compensation amount $\Delta\theta_r$ is added, and thus the observation of the rotor flux can be realized. where,

$$\Delta\theta_r=-\arctan(\frac{\omega_r}{\omega_{cf}})\tag{44}$$

$$\hat{\theta}_r=\arctan\frac{\psi_{r\beta}}{\psi_{r\alpha}}+\frac{(-\psi_{r\alpha}+|\psi_{r\alpha}|)\times\pi/2}{|\psi_{r\alpha}|}\tag{45}$$

where, ω_{cf} is the cut-off frequency of low pass filter.

According to the equivalent sliding mode function and the flux linkage in the two-phase stationary coordinate system, the rotor angular velocity is obtained. Further, (41) are converted to

$$\begin{cases}\lambda_{r\alpha}^{eq}=\eta\hat{\psi}_{r\alpha}+\omega_r\hat{\psi}_{r\beta}-\eta L_{m\alpha}i_{s\alpha}\\ \lambda_{r\beta}^{eq}=\eta\hat{\psi}_{r\beta}-\omega_r\hat{\psi}_{r\alpha}-\eta L_{m\beta}i_{s\beta}\end{cases}\tag{46}$$

where, $\eta=1/\tau_r$.

The two sides of the first row in (46) are multiplied by $\hat{\psi}_{r\beta}$, and the second line is multiplied by $\hat{\psi}_{r\alpha}$

$$\begin{cases} \hat{\psi}_{r\beta}\lambda_{r\alpha}^{eq} = \eta\hat{\psi}_{r\alpha}\hat{\psi}_{r\beta} + \omega_r\hat{\psi}_{r\beta}^2 - \eta L_{m\alpha}i_{s\alpha}\hat{\psi}_{r\beta} \\ \hat{\psi}_{r\alpha}\lambda_{r\beta}^{eq} = \eta\hat{\psi}_{r\beta}\hat{\psi}_{r\alpha} - \omega_r\hat{\psi}_{r\alpha}^2 - \eta L_{m\beta}i_{s\beta}\hat{\psi}_{r\alpha} \end{cases} \tag{47}$$

From (47) , the estimated speed can be written as

$$\hat{\omega}_r = \frac{\hat{\psi}_{r\beta}\lambda_{r\alpha}^{eq} - \hat{\psi}_{r\alpha}\lambda_{r\beta}^{eq} - \eta(i_{s\beta}\hat{\psi}_{r\alpha}L_{m\beta} - i_{s\alpha}\hat{\psi}_{r\beta}L_{m\alpha})}{\hat{\psi}_{r\alpha}^2 + \hat{\psi}_{r\beta}^2} \tag{48}$$

According to (48), the speed estimation formula under open-phase fault includes the mutual inductance component of the $\alpha\beta$ axis. When the machine is in normal state, there is $L_{m\alpha} = L_{m\beta} = L_m$, and the speed estimation formula degenerate into "healthy" state.

The control structure diagram of the sensorless fault-tolerant control system for SPIM is shown in Fig. 4, where, the current controller in d-axis and q-axis is PI controller, which in z-axis is QPR controller. The i_d^*, i_d and u_d^* is the d-axis reference current, feedback current and reference voltage respectively. The i_q^*, i_q and u_q^* is the q-axis reference current, feedback current and reference voltage respectively. The i_z^*, i_z and u_z^* is the z-axis reference current, feedback current and reference voltage respectively. The motor is powered by two parallel three phase two level voltage source inverters. By using SMO to replace the traditional encoder, the cost is reduced, and backup protection is provided after the encoder is damaged, which greatly improves the reliability of the drive system. When the SPIM is running under normal state, the SVPWM based on zero-sequence balance is adopted to reduce the harmonics of stator current [25]. Because the space voltage vector is irregular and its amplitude is not uniform when open-phases fault occurs, it is difficult to realize the SVPWM based on zero-sequence balance. The post-fault SVPWM adopts based on virtual action time [26]. Compared with the current hysteresis modulation strategy adopted in the optimal fault-tolerant current control, the switching frequency is fixed and the torque ripple is reduced, which can be used in high-power applications. When a failure occurs, the post-fault SVPWM can be used to generate a continuous rotation of the voltage vector and reduce the torque ripple.

B. OBSERVER STABILITY ANALYSIS

The stability of the current observer in Part A is guaranteed by selecting the appropriate sliding mode gain K. The Lyapunov function [27] for the proposed sliding mode current observer is chosen as

$$V = \boldsymbol{S}_n^T\boldsymbol{S}_n \tag{49}$$

where, $\boldsymbol{S}_n$ is the error between observing current and actual current. $\boldsymbol{S}_n = \begin{bmatrix} S_{\alpha s} & S_{\beta s} \end{bmatrix}^T$, $S_\alpha = \hat{i}_{s\alpha} - i_{s\alpha}$, $S_\beta = \hat{i}_{s\beta} - i_{s\beta}$.

Combying (38) and (39), The differentiation of $\boldsymbol{S}_n$ can be expressed as

$$p\boldsymbol{S}_n = \begin{bmatrix} pS_\alpha \\ pS_\beta \end{bmatrix} = \begin{bmatrix} p(\hat{i}_{s\alpha} - i_{s\alpha}) \\ p(i_{s\beta} - i_{s\beta}) \end{bmatrix} \tag{50}$$

$$\begin{cases} pS_\alpha = \epsilon_\alpha(e_{r\alpha} - K_\alpha S_\alpha - \dfrac{L_r R_s}{L_{m\alpha}}S_\alpha) \\ pS_\beta = \epsilon_\beta(e_{r\beta} - K_\beta S_\beta - \dfrac{L_r R_s}{L_{m\beta}}S_\beta) \end{cases} \tag{51}$$

Consider that

$$(p\boldsymbol{S}_n^T\boldsymbol{S}_n)^T = \boldsymbol{S}_n^T p\boldsymbol{S}_n \tag{52}$$

The Lyapunov function V is obviously positive definite and satisfies the first condition of Lyapunov stability. It is known from the second conditions of Lyapunov stability that if the first derivative of the Lyapunov function is less than 0, as is shown in (53), the sliding mode observer of the current surface of the above analysis is stable.

$$\begin{aligned} pV = 2\boldsymbol{S}_n^T p\boldsymbol{S}_n = 2\epsilon_\alpha S_\alpha\left[e_{r\alpha} - S_\alpha(K_\alpha + \frac{L_r R_s}{L_{m\alpha}})\right] \\ +2\epsilon_\beta S_\beta\left[e_{r\beta} - S_\beta(K_\beta + \frac{L_r R_s}{L_{m\beta}})\right] < 0 \end{aligned} \tag{53}$$

The sliding mode gain K can be expressed as

$$\begin{cases} K_\alpha > \dfrac{S_\alpha e_{r\alpha}}{S_\alpha^2} - \dfrac{L_r R_s}{L_{m\alpha}} \\ K_\beta > \dfrac{S_\beta e_{r\beta}}{S_\beta^2} - \dfrac{L_r R_s}{L_{m\beta}} \end{cases} \tag{54}$$

$$K > max(K_\alpha, K_\beta) \tag{55}$$

A proper K is selected to ensure the stability of the system and to generate the sliding mode motion. The block diagram of sliding mode flux linkage and speed estimation is shown in Fig. 5, where I_{rem} and U_{rem} are the phase voltage and phase current of the remaining effective phase respectively.

V. SIMULATION AND EXPERIMENTAL RESULTS

A. SIMULATION RESULTS

To verify the accuracy of the proposed sensorless fault-tolerant control for SPIM Based on SMO, a simulation module in MATLAB/Simulink is built. The structure diagram of sensorless field oriented control of six-phase induction machine under open-phases faults is shown in Fig. 4, the motor is powered by two parallel three-phase voltage source inverters. The main parameters of the SCIM drive are given in Table 2.

In order to verify the validity and correctness of the proposed SMO speed sensorless fault-tolerant control method, three kinds of open circuit fault conditions are simulated. The total simulation time is 0.8s, the reference speed is set to 500r/min, the load torque is switched from no load to 10N·m at 0.1s, the open circuit fault occurs at 0.4s, and the fault-tolerant control strategy is adopted at 0.5s.

Fig. 6 is the simulation waveform of sensorless fault-tolerant control when the motor transits from normal state to sudden single-phase open-circuit fault. Fig. 7 is the simulation waveform of sensorless fault-tolerant control when the machine transits from normal state to sudden two-phase open-circuit fault. It can be seen from the waveform that

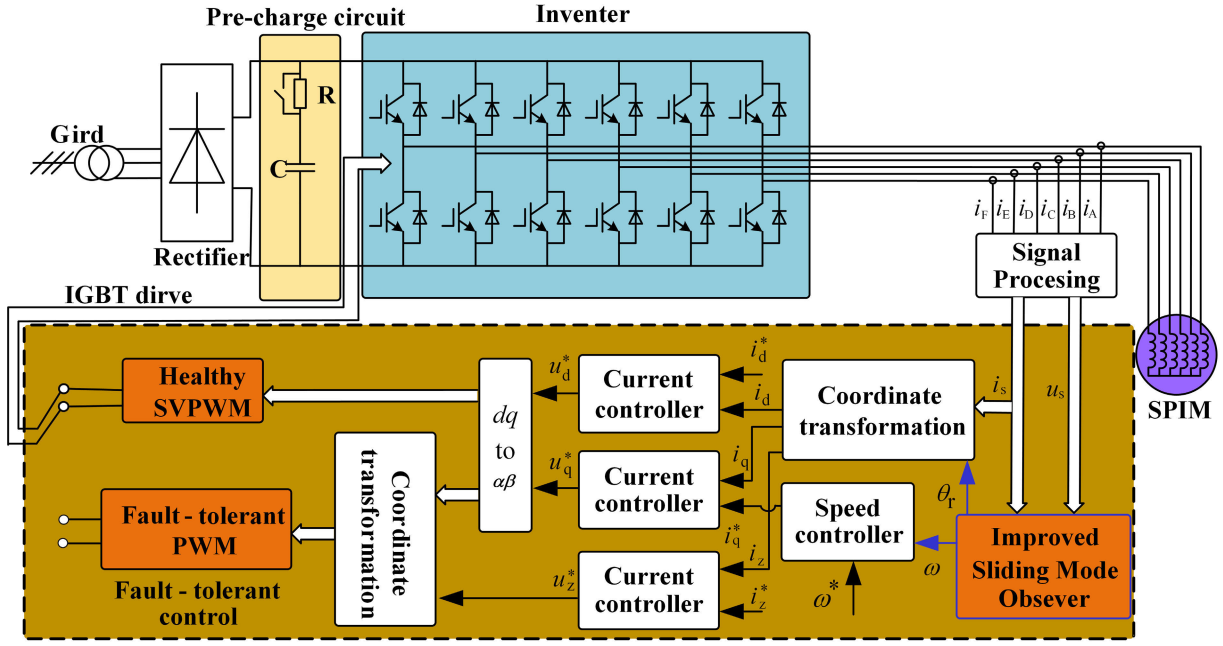

FIGURE 4. The diagram of sensorless field oriented control of SPIM under open-phases fault.

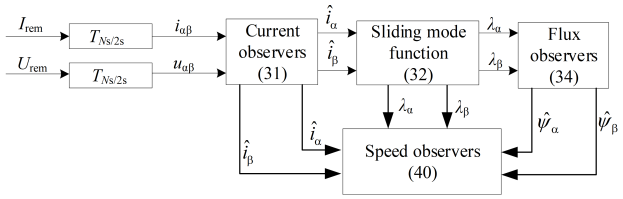

FIGURE 5. Sliding mode flux and speed observer block diagram.

TABLE 2. The parameters of SPIM .

Parameters	Values	Parameters	Values
DC source voltage (V)	311	Rotor resistance (Ω)	1.62
Number of pole-pairs	3	Stator inductance (mH)	444
Inertia (kg · m^2)	0.02	Rotor inductance (mH)	444
Stator resistance (Ω)	2.125	Mutual inductance (mH)	434

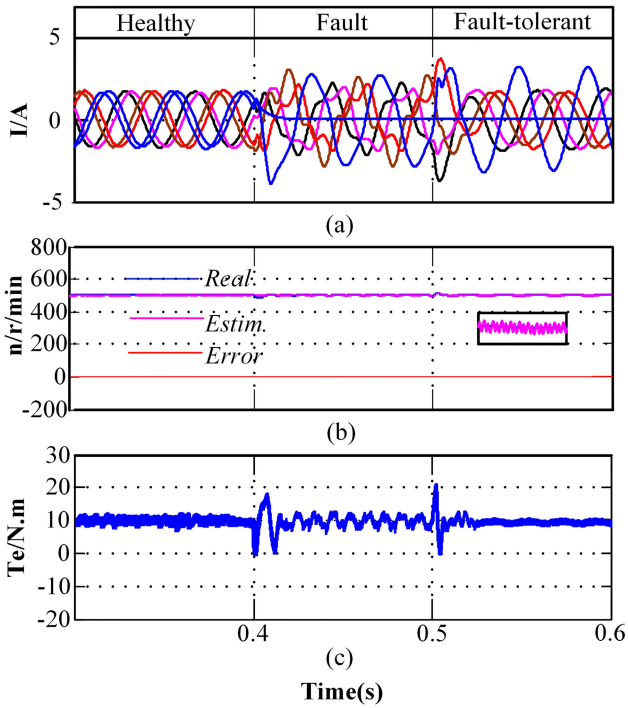

FIGURE 6. Dynamic performances under healthy, single-phase fault and fault-tolerant condition. (a) Current. (b) Actual speed and observational speed. (c) Torque.

when single-phase open-circuit fault occurs, torque waveform appears double-frequency fluctuation with amplitude of about 5N·m, and the resultant speed fluctuation is consistent with the theory when single-phase open-circuit fault occurs [9], the fault phase current is zero, other phase currents are asymmetrical, the amplitude increases and the distortion is serious.

The improved SMO can still identify the speed accurately after phase failure. The estimated value and the actual value of the motor tend to be same, and the error is very small. The strategy is switched to the corresponding fault-tolerant control strategy at 0.5s, the sinusoidal waveform of residual phase current is well, the torque and speed fluctuations are reduced, and the waveform tends to be stable. In single-phase open circuit, the maximum one-phase current is close to 4.5A, and the minimum current is close to 2A, which is smaller

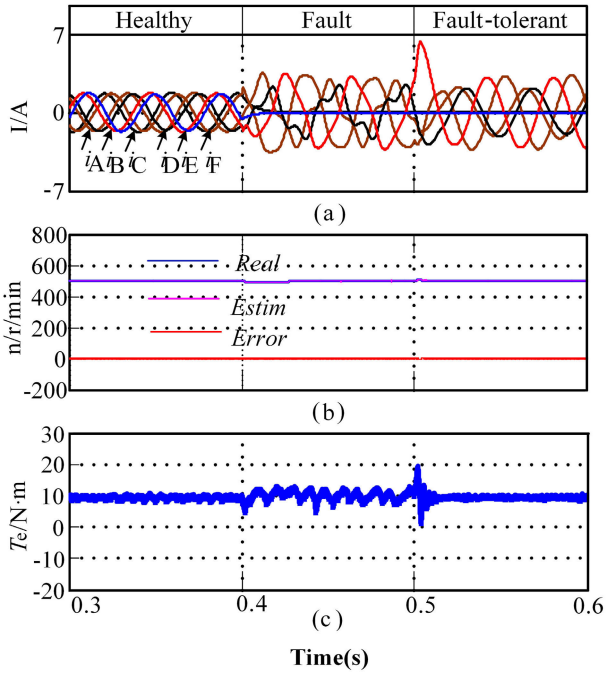

FIGURE 7. Dynamic performances under healthy, two-phase fault and fault-tolerant condition. (a) Current. (b) Actual speed and observational speed. (c) Torque.

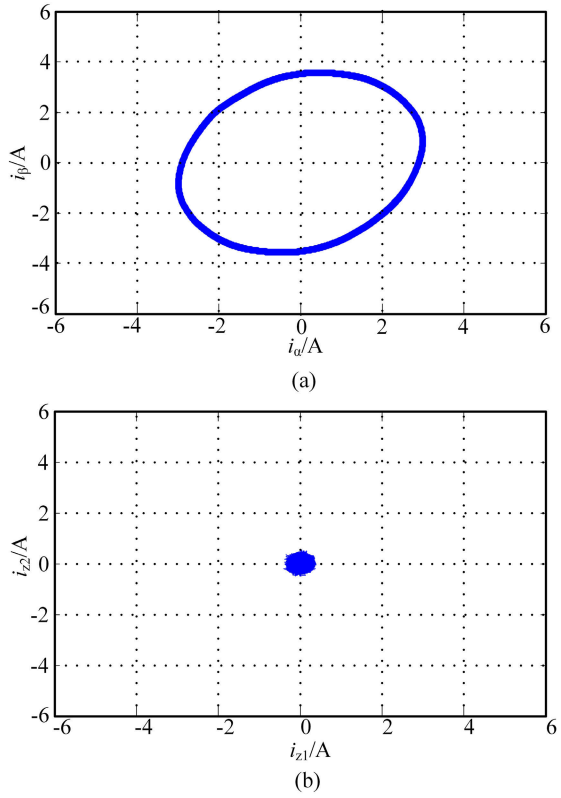

FIGURE 8. Fundamental plane and harmonic plane current trajectories under single-phase open circuit. (a) $\alpha-\beta$ plane current trajectory. (b) z_1-z_2 plane current trajectory.

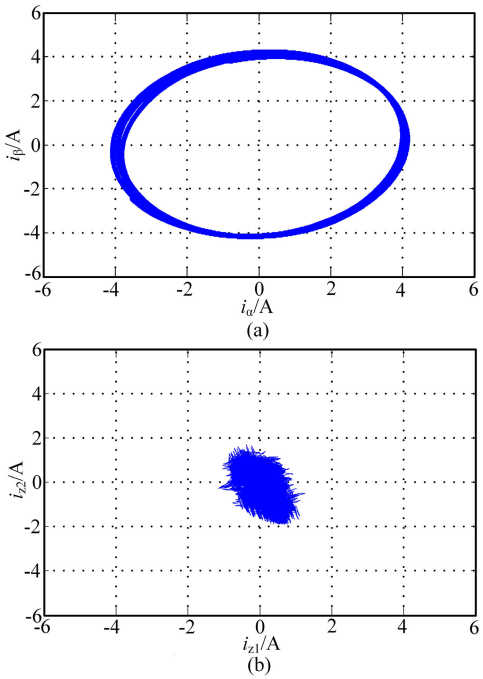

FIGURE 9. Fundamental plane and harmonic plane current trajectories under two-phase open circuit. (a) $\alpha-\beta$ plane current trajectory. (b) z_1-z_2 plane current trajectory.

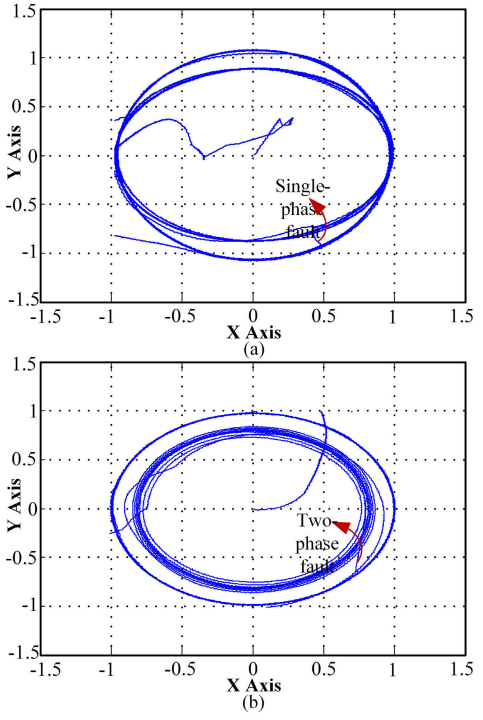

FIGURE 10. Stator flux trajectory. (a) Healthy and single-phase fault. (b) Healthy and two-phase fault.

than the current before fault-tolerant control. Compared with single-phase open-circuit faults, the torque and speed fluctuations are greater in two-phase open-circuit faults. Among the remaining four-phase stator currents, the maximum current amplitude is close to 4.8A and the minimum current amplitude is close to 3.3A. Compared with one-phase open-circuit faults, the current amplitude increases, and the

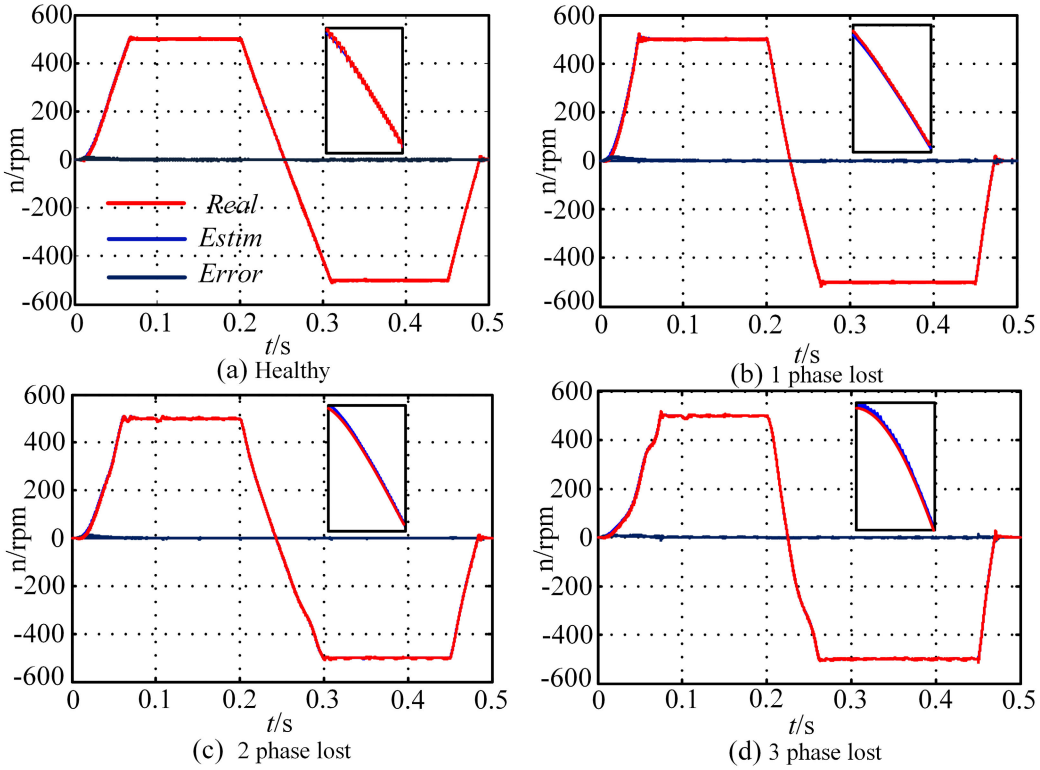

FIGURE 11. Sensorless speed control of the SPIM under healthy and open-phases faults. (a) Healthy. (b) Single-phase fault. (c) Two-phase fault. (d) Three-phase fault.

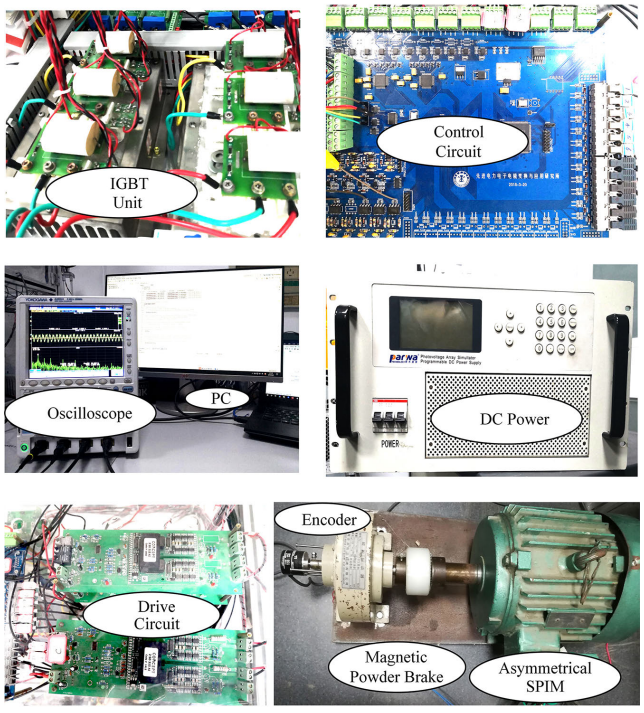

FIGURE 12. Experiment platform of the six-phase induction machine.

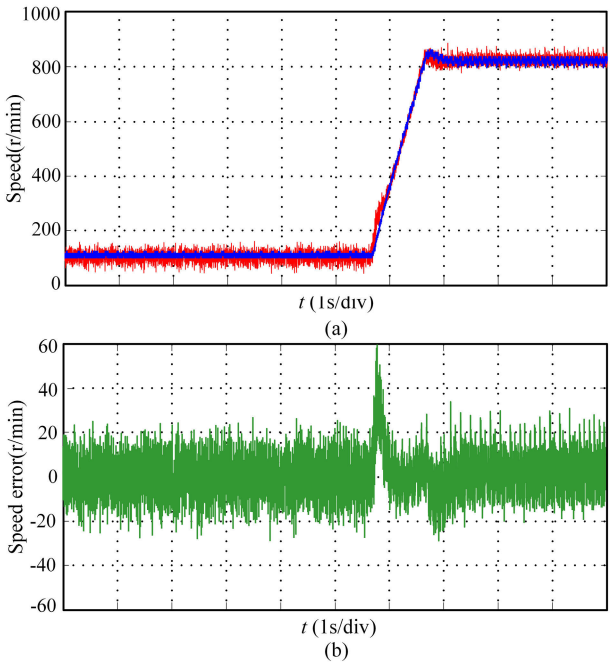

FIGURE 13. Experimental results of six-phase induction machine speed identification under normal condition based on SMO. (a) Speed of no-load start up. (b) Speed error.

power of each phase increases, which indicates that the current needs to be increased to maintain the output power unchanged.

Fig. 8 and Fig. 9 are the fundamental plane and harmonic plane current trajectories of single-phase and two-phase open-circuit under steady-state respectively. It can be

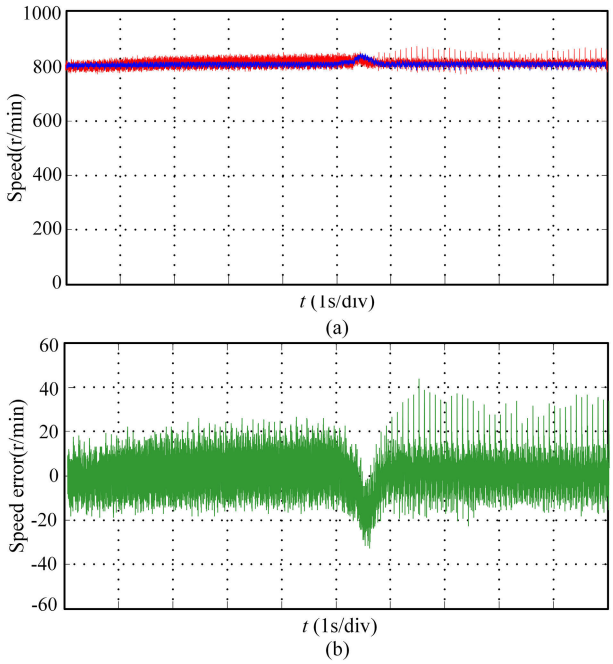

FIGURE 14. Experimental results of six-phase induction machine speed identification under normal condition based on SMO. (a) Speed from rated load to no load. (b) Speed error.

seen that the fundamental plane current trajectory is elliptical, which indicates that the amplitude of the $\alpha-\beta$ axis current is different, the harmonic plane amplitude is much smaller than the fundamental plane amplitude and the PR regulator has a good suppression effect on the harmonic plane current.

Fig. 10 is the stator flux linkage of the motor. When phase failure occurs, the flux linkage changes from circular to elliptical, which is consistent with the asymmetry of the flux equation on the $\alpha-\beta$ axis.

The experimental platform shown in Fig. 12 is built to further verify the ability of speed-sensorless fault-tolerant control strategy in tracking speed and resisting load disturbance. The reference speed of the control system is set to 500 rpm at $t = 0$ s, and set to -500 rpm at $t = 0.2$ s. When the system is stable, the load will suddenly increase from 0 to 10N·m. Fig. 11 is a dynamic response waveform of motor speed in case of motor health or single-phase, two-phase and three-phase open-circuit faults, including the actual and estimated values of rotor speed and the errors between them. The simulation results show that the proposed SMO can accurately estimate the speed of the motor under open-phase fault, with high accuracy, strong ability to track the sudden change of speed, and high robustness to motor parameters and load conditions.

B. EXPERIMENTAL TEST

The sensorless fault-tolerant control schemes for six-phase induction machine have been verified by simulation. To further verify the feasibility of the proposed scheme, the corresponding experimental verification is carried out.

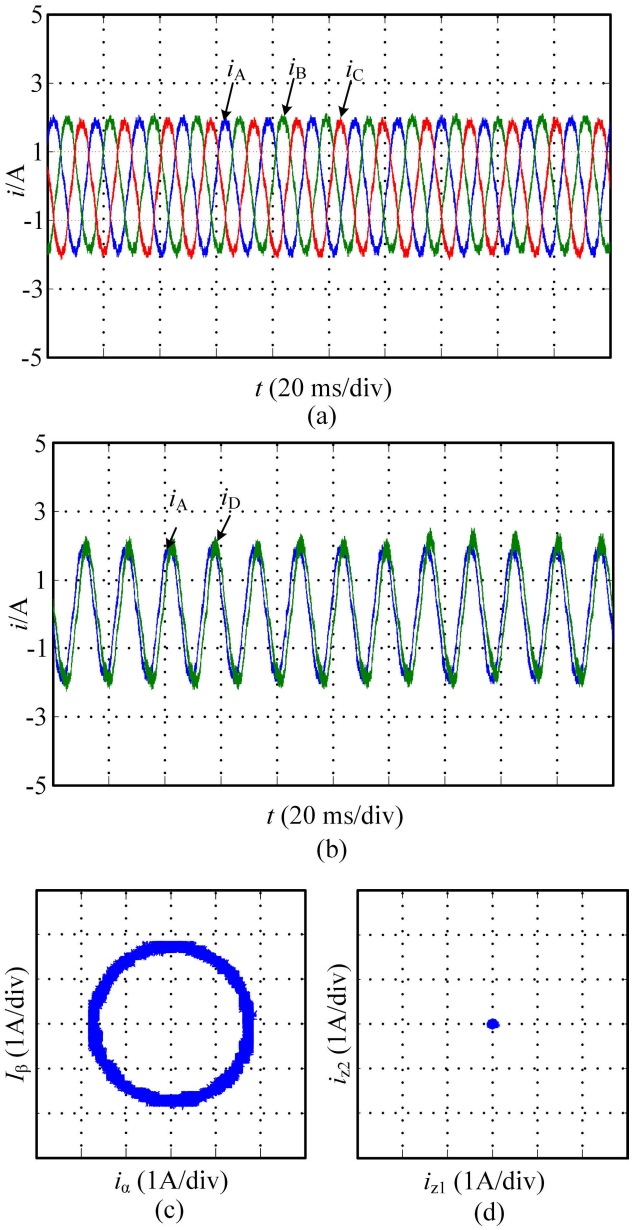

FIGURE 15. Experimental results of six-phase induction machine stator current under normal condition based on SMO. (a) Phase current of A, B and C. (b) Phase Current of A and D. (c) $\alpha-\beta$ plane current trajectory. (d) z_1-z_2 plane current trajectory.

The machine used in the experiment is an asymmetric squirrel cage type six-phase induction motor. A 2000 pulses encoder is installed on the mechanical shaft to obtain real-time rotational speed data as a criterion for speed identification. The rated voltage of the stator is 190V, the rated current is 7.4A, the number of pole-pairs is 3, the rated speed is 970r/min. The switching frequency is set to 10 kHz. The experimental platform is shown in Fig. 12. The control system platform mainly consists of two parts: the power circuit and the control circuit. IGBT is used as the switching device of the power circuit, and the DC voltage is 190 V. The core control chip is TMS320F28335. A magnetic powder brake

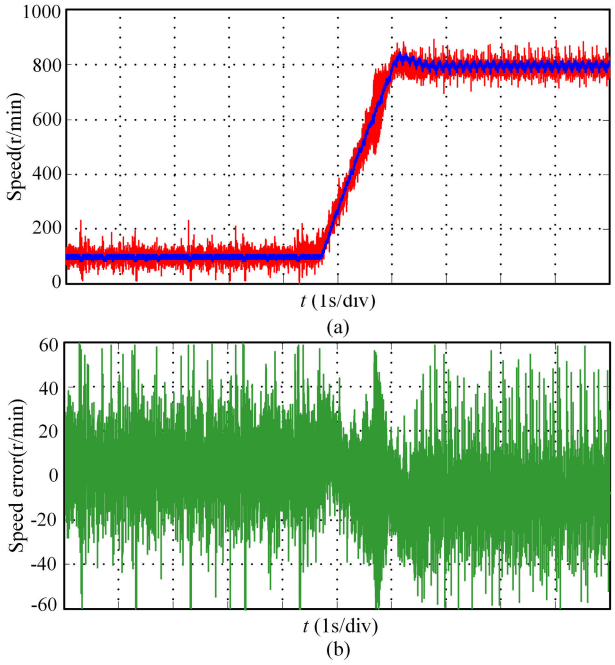

FIGURE 16. Experimental results of six-phase induction machine speed identification under single-phase fault condition based on SMO. (a) Speed of no-load start up. (b) Speed error.

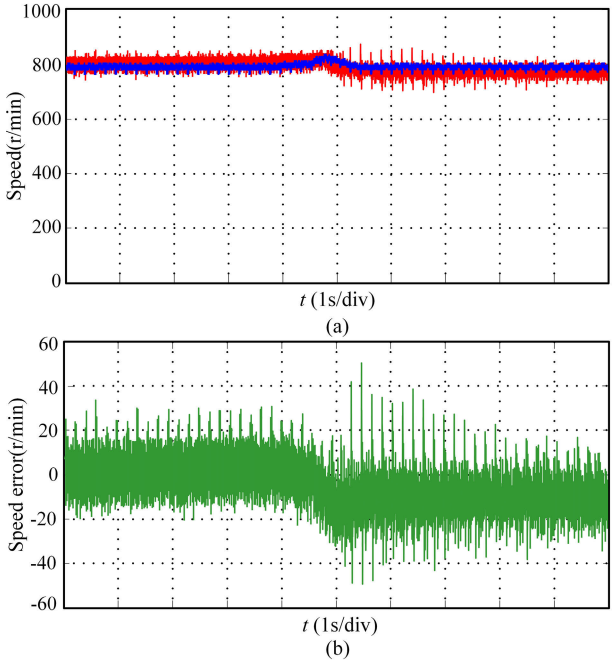

FIGURE 17. Experimental results of six-phase induction machine speed identification under single-phase fault condition condition based on SMO. (a) Speed from rated load to no load. (b) Speed error.

with a maximum braking torque of 20N·m is used as the load of the motor. a four-channel oscilloscope is used to collect the output waveform of the motor such as speed, torque and phase current.

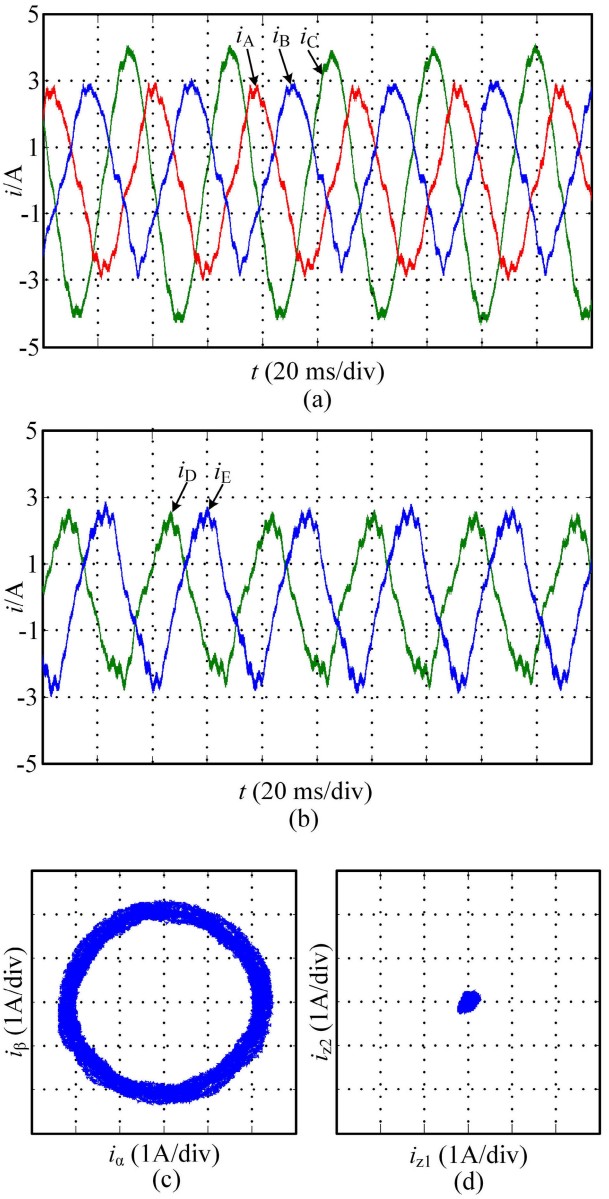

FIGURE 18. Experimental results of six-phase induction machine stator current under single-phase open-circuit fault based on SMO. (a) Phase current of A, B and C. (b) Phase Current of A and D. (c) $\alpha-\beta$ plane current trajectory. (d) z_1-z_2 plane current trajectory.

In order to verify the validity of the speed-sensorless fault-tolerant control strategy based on sliding mode observer, the reference speed of the motor is set at 500 r/min, and the rated load torque is added after the system is stabilized.

Fig. 13 is the speed identification results of no-load start under normal operation. Fig. 14 is the speed identification results from rated-load to no-load under normal operation. Among them, (a) and (b) are the speed identification results and speed error of the motor. The blue track is the actual value of the speed and the red track is the observed value of the speed. By choosing the optimal current sliding mode gain K and the saturation width Δ, the chattering of the system

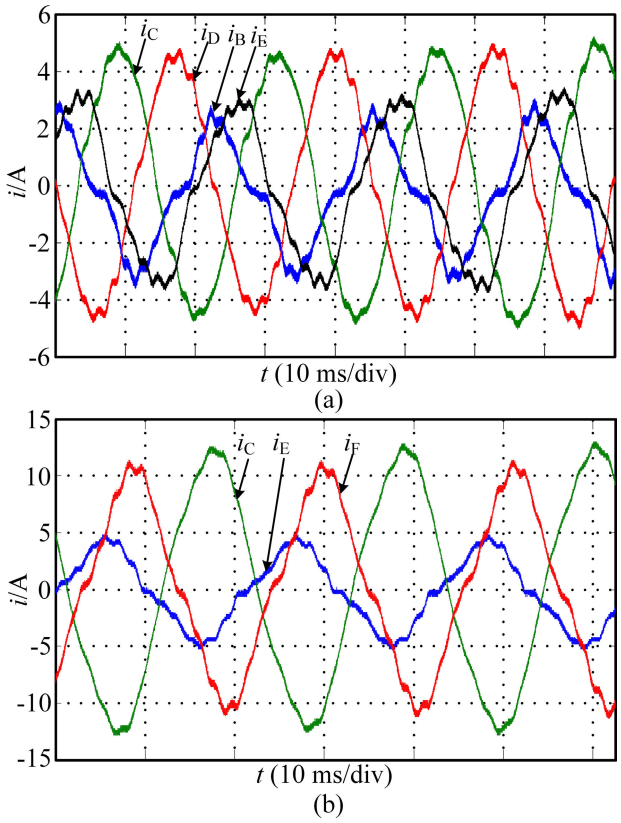

FIGURE 19. Experiments result of phase current under two and three-phase open circuits. (a) A and F phase open-circuit phase current. (b) A, B and D phase open-circuit phase current.

can be greatly reduced. The experimental waveforms shows that the purposed improved observer can accurately identify the speed of the motor with minimal observation error, small chattering phenomenon and strong robustness to load. Fig. 15 is the result of current operation under normal operation, (a) is the three-phase stator current of A, B and C, and (b) is the two-phase stator current of A and D. The harmonic content of current waveform is less and the phase is correct. (c) and (d) are the current trajectory of fundamental wave and harmonic. The fundamental current trajectory wave is circular, and the amplitude of fundamental current is much larger than that of harmonic plane.

Fig. 16 is the result of speed identification and speed error of no-load start under single-phase open-circuit operation. Fig. 17 is the result of speed identification and speed error from rated-load to no-load under single-phase open-circuit operation. The motor speed can be observed even when the motor is in one-phase open-circuit fault. Fig. 18 is the result of current operation when the motor is in one-phase open-circuit operation. Among them, (a) is the three-phase stator phase currents of A, B and C, and (b) is the two-phase stator phase currents of D and E. The harmonic content of current waveform is small, and the phase is consistent with simulation. (c), (d) are the current trajectory when the motor is in one-phase open-circuit operation. The trajectory of harmonic plane current is elliptical when the phase is absent, and the amplitude is much larger than that of harmonic plane. The current amplitude of the motor under single-phase open-circuit fault is larger than that under normal condition, and the phase difference of each phase current is consistent with the simulation. The amplitude of the harmonic current is significantly smaller than that of the fundamental current, which verifies the control effect of PR regulator. The speed identification results of motor in two-phase open circuit and three-phase open circuit are similar to those in Fig. 16 and this paper will not go into detail. Fig. 19 is the current steady state diagram of motor in two-phase open circuit and three-phase open circuit respectively. The experimental results are in coincident with the simulation results. From the experimental results of sensorless fault-tolerant control under three kinds of faults, it can be seen that the method proposed in this paper can realize sensorless fault-tolerant control of any phase failure.

VI. CONCLUSIONS

The proposed fault-tolerant speed sensorless control strategy for six-phase induction machine has the advantages of high accuracy, simple structure, easy adjustment of parameters and high reliability under sensorless operation. Vector control after phase failure is realized in the fundamental wave plane, and odd harmonics are suppressed in the harmonic plane. By modifying the sliding mode observer, it can satisfy the fault tolerance operation. The simulation and experiment results show that the proposed speed sensorless fault-tolerant control method of six-phase induction motor has good fault-tolerant ability, tracking performance and strong robustness, and suitable for high performance and high reliability driving occasions. It is obvious to see that the proposed method can be extended to the speed sensorless fault-tolerant control for any type of multiphase induction motor in the case of open fault.

REFERENCES

[1] W. Cao, B. C. Mecrow, G. J. Atkinson, J. W. Bennett, and D. J. Atkinson, "Overview of electric motor technologies used for more electric aircraft (MEA)," *IEEE Trans. Ind. Electron.*, vol. 59, no. 9, pp. 3523–3531, Sep. 2012.

[2] Y. Zhao and T. A. Lipo, "Modeling and control of a multi-phase induction machine with structural unbalance," *IEEE Trans. Energy Convers.*, vol. 11, no. 3, pp. 570–577, Sep. 1996.

[3] M. Taherzadeh, S. Carriere, M. Joorabian, F. Betin, R. Kianinezhad, and G. A. Capolino, "Analysis and control of six-phase induction machines in unbalanced operating situation due to phase opening," in *Proc. 40th Annu. Conf. IEEE Ind. Electron. Soc. (IECON)*, Dallas, TX, USA, Oct./Nov. 2014, pp. 417–423.

[4] M. Bermudez, I. Gonzalez-Prieto, F. Barrero, H. Guzman, M. J. Duran, and X. Kestelyn, "Open-phase fault-tolerant direct torque control technique for five-phase induction motor drives," *IEEE Trans. Ind. Electron.*, vol. 64, no. 2, pp. 902–911, Feb. 2017.

[5] M. H. Holakooie, M. Ojaghi, and A. Taheri, "Modified DTC of a six-phase induction motor with a second-order sliding-mode mras-based speed estimator," *IEEE Trans. Power Electron.*, vol. 34, no. 1, pp. 600–611, Jan. 2019.

[6] H. A. Toliyat, "Analysis and simulation of five-phase variable-speed induction motor drives under asymmetrical connections," *IEEE Trans. Power Electron.*, vol. 13, no. 4, pp. 748–756, Jul. 1998.

[7] A. Mohammadpour and L. Parsa, "Global fault-tolerant control technique for multiphase permanent-magnet machines," *IEEE Trans. Ind. Appl.*, vol. 51, no. 1, pp. 178–186, Jan./Feb. 2015.

[8] A. Tani, M. Mengoni, L. Zarri, G. Serra, and D. Casadei, "Control of multiphase induction motors with an odd number of phases under open-circuit phase faults," *IEEE Trans. Power Electron.*, vol. 27, no. 2, pp. 565–577, Feb. 2012.

[9] R. Kianinezhad, B. Nahid-Mobarakeh, L. Baghli, F. Betin, and G.-A. Capolino, "Modeling and control of six-phase symmetrical induction machine under fault condition due to open phases," *IEEE Trans. Ind. Electron.*, vol. 55, no. 5, pp. 1966–1977, May 2008.

[10] H. Guzman, M. J. Duran, F. Barrero, B. Bogado, and S. Toral, "Speed control of five-phase induction motors with integrated open-phase fault operation using model-based predictive current control techniques," *IEEE Trans. Ind. Electron.*, vol. 61, no. 9, pp. 4474–4484, Sep. 2014.

[11] F. Barrero, J. Prieto, E. Levi, R. Gregor, S. Toral, M. J. Duran, and M. Jones, "An enhanced predictive current control method for asymmetrical six-phase motor drives," *IEEE Trans. Ind. Electron.*, vol. 58, no. 8, pp. 3242–3252, Aug. 2011.

[12] X. Sun, C. Hu, J. Zhu, S. Wang, W. Zhou, Z. Yang, G. Lei, K. Li, B. Zhu, and Y. Guo, "MPTC for PMSMs of EVs with multi-motor driven system considering optimal energy allocation," *IEEE Trans. Magn.*, vol. 55, no. 7, Jul. 2019, Art. no. 8104306.

[13] X. Sun, L. Chen, H. Jiang, Z. Yang, J. Chen, and W. Zhang, "High-performance control for a bearingless permanent-magnet synchronous motor using neural network inverse scheme plus internal model controllers," *IEEE Trans. Ind. Electron.*, vol. 63, no. 6, pp. 3479–3488, Jun. 2016.

[14] X. Sun, Z. Shi, L. Chen, and Z. Yang, "Internal model control for a bearingless permanent magnet synchronous motor based on inverse system method," *IEEE Trans. Energy Convers.*, vol. 31, no. 4, pp. 1539–1548, Dec. 2016.

[15] X. Sun, C. Hu, G. Lei, Y. Guo, and J. Zhu, "State feedback control for a PM hub motor based on grey wolf optimization algorithm," *IEEE Trans. Power Electron.*, to be published.

[16] X. Sun, L. Chen, Z. Yang, and H. Zhu, "Speed-sensorless vector control of a bearingless induction motor with artificial neural network inverse speed observer," *IEEE/ASME Trans. Mechatronics*, vol. 18, no. 4, pp. 1357–1366, Aug. 2013.

[17] R. Bojoi, G. Griva, and F. Profumo, "Field oriented control of dual three-phase induction motor drives using a Luenberger flux observer," in *Proc. Conf. Rec. IEEE Ind. Appl. Conf. 41st IAS Annu. Meeting*, Tampa, FL, USA, Oct. 2006, pp. 1253–1260.

[18] R. Gregor and J. Rodas, "Speed sensorless control of dual three-phase induction machine based on a luenberger observer for rotor current estimation," in *Proc. 38th Annu. Conf. IEEE Ind. Electron. Soc. (IECON)*, Montreal, QC, Canada, Oct. 2012, pp. 3653–3658.

[19] L. Sheng, G. Xiaojie, and Z. Lanyong, "Robust adaptive backstepping sliding mode control for six-phase permanent magnet synchronous motor using recurrent wavelet fuzzy neural network," *IEEE Access*, vol. 5, pp. 14502–14515, 2017.

[20] A. S. Morsy, A. S. Abdel-khalik, S. Ahmed, and A. Massoud, "Sensorless field oriented control of five-phase induction machine under open-circuit phase faults," in *Proc. IEEE Energy Convers. Congr. Expo.*, Denver, CO, USA, Sep. 2013, pp. 5112–5117.

[21] M. Taherzadeh, M. Joorabian, S. Carriere, R. Kianinezhad, and F. Betin, "Speed adaptive flux Luenberger observer used in sensorless vector control of an unbalanced six-phase induction machine," in *Proc. 5th Annu. Int. Power Electron., Drive Syst. Technol. Conf. (PEDSTC)*, Tehran, Iran, Feb. 2014, pp. 1–6.

[22] W. Kong, J. Huang, B. Li, M. Kang, and L. Zhao, "Improved sliding-mode observer for sensorless control of five-phase induction motor," in *Proc. Int. Conf. Elect. Mach. Syst. (ICEMS)*, Busan, South Korea, Oct. 2013, pp. 2024–2027.

[23] L. Zhang, Y. Fan, C. Li, A. Nied, and M. Cheng, "Fault-tolerant sensorless control of a five-phase FTFSCW-IPM motor based on a wide-speed strong-robustness sliding mode observer," *IEEE Trans. Energy Convers.*, vol. 33, no. 1, pp. 87–95, Mar. 2018.

[24] H. S. Che, M. J. Duran, E. Levi, M. Jones, W.-P. Hew, and N. A. Rahim, "Postfault operation of an asymmetrical six-phase induction machine with single and two isolated neutral points," *IEEE Trans. Power Electron.*, vol. 29, no. 10, pp. 5406–5416, Oct. 2014.

[25] Y. Zhao and T. A. Lipo, "Space vector PWM control of dual three-phase induction machine using vector space decomposition," *IEEE Trans. Ind. Appl.*, vol. 31, no. 5, pp. 1100–1109, Sep./Oct. 1995.

[26] D.-W. Chung, J.-S. Kim, and S.-K. Sul, "Unified voltage modulation technique for real-time three-phase power conversion," *IEEE Trans. Ind. Appl.*, vol. 34, no. 2, pp. 374–380, Mar. 1998.

[27] H. Rehman, A. Derdiyok, M. K. Guven, and L. Xu, "A new current model flux observer for wide speed range sensorless control of an induction machine," *IEEE Trans. Power Electron.*, vol. 17, no. 6, pp. 1041–1048, Nov. 2002.

[28] V. I. Utkin, "Sliding mode control design principles and applications to electric drives," *IEEE Trans. Ind. Electron.*, vol. 40, no. 1, pp. 23–36, Feb. 1993.

[29] X. Sun, Y. Shen, S. Wang, G. Lei, Z. Yang, and S. Han, "Core losses analysis of a novel 16/10 segmented rotor switched reluctance BSG motor for HEVs using nonlinear lumped parameter equivalent circuit model," *IEEE/ASME Trans. Mechatronics*, vol. 23, no. 2, pp. 747–757, Apr. 2018.

[30] M. S. Zaky, M. K. Metwaly, H. Z. Azazi, and S. A. Deraz, "A new adaptive smo for speed estimation of sensorless induction motor drives at zero and very low frequencies," *IEEE Trans. Ind. Electron.*, vol. 65, no. 9, pp. 6901–6911, Sep. 2018.

[31] H. Wang, X. Ge, and Y.-C. Liu, "Second-order sliding-mode MRAS observer-based sensorless vector control of linear induction motor drives for medium-low speed maglev applications," *IEEE Trans. Ind. Electron.*, vol. 65, no. 12, pp. 9938–9952, Dec. 2018.

[32] L. Sheng, W. Li, Y. Wang, M. Fan, and X. Yang, "Sensorless control of a shearer short-range cutting interior permanent magnet synchronous motor based on a new sliding mode observer," *IEEE Access*, vol. 5, pp. 18439–18450, 2017.

YIWEN GENG was born in Jiangsu, China, in 1977. He received the B.S., M.S., and Ph.D. degrees from the School of Electrical and Power Engineering, China University of Mining and Technology, Xuzhou, China, in 2000, 2004, and 2014, respectively. From 2006 to 2016, he was a Lecturer with the School of Electrical and Power Engineering, China University of Mining and Technology. Since 2016, he has been with the Department of School of Electrical and Power Engineering, China University of Mining and Technology, where he is currently an Associate Professor. His current research interests include motor control, photovoltaic inverters, and power electronics.

ZOU LAI was born in Henan, China, in 1993. He received the B.S. degree from the College of Electrical Engineering and Control Science, Nanjing Tech University, Nanjing, China, in 2017. He is currently pursuing the M.S. degree in electrical engineering with the School of Electrical and Power Engineering, China University of Mining and Technology, Xuzhou, China. His current research interests include sensorless and fault tolerant control of multiphase motor.

YONGGANG LI was born in 1994. He received the B.S. degree from the School of Electrical and Electronic Engineering, Shanghai Institute of Technology, Shanghai, China, in 2015, and the M.S. degrees from the China University of Mining and Technology, Xuzhou, China, in 2019. His research interests include analysis and control of multiphase machine driving system, direct-drive, and doubly fed wind power converter control.

DING WANG was born in Henan, China, in 1994. He received the B.S. degree in electrical engineering and automation from Northwest A&F University, Yangling, China, in 2017. He is currently pursuing the M.S. degree in electrical engineering with the School of Electrical and Power Engineering, China University of Mining and Technology, Xuzhou, China. His research interest includes in the area of multiphase motor drive.

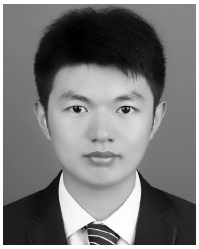

RUICHENG CHEN was born in Jiangsu, China, in 1992. He received the B.S. and M.S. degrees in electrical engineering from the China University of Mining and Technology, Xuzhou, China, in 2015 and 2018, respectively. He is currently with the China University of Mining and Technology, Xuhai College, where he is currently a Lecturer. His current research interests include the new energy electric vehicles and related technologies.

PENGFEI ZHENG was born in Anhui, China, in 1993. He received the B.S. degree in electrical engineering and automation from the Nanjing University of Posts and Telecommunications, Xuzhou, China, in 2016, and the M.S. degree from the China University of Mining and Technology, Xuzhou, in 2019. His current research interests include a bidirectional three-level LLC resonant converter and its control.